Key Points:
- Agricultural soil was the largest source contribution and accounted for 29.6% of the YRD CH$_4$ budget during our study period
- The overestimation was contributed by agricultural soils (rice cultivation) and fuel exploitation
- The emission estimates were 30.2($\pm$17.6)%, 31.5%, and 30.8% lower than the a priori EDGAR v432 emission inventory estimate

Correspondence to:
C. Hu, T. J. Griffis, and X. Lee,
huxxx991@umn.edu;
timgriffis@umn.edu;
xuhui.lee@yale.edu

Anthropogenic Methane Emission and Its Partitioning for the Yangtze River Delta Region of China

Cheng Hu[1,2,3] (iD), Timothy J. Griffis[3] (iD), Shoudong Liu[2], Wei Xiao[2] (iD), Ning Hu[2], Wenjing Huang[2], Dong Yang[4], and Xuhui Lee[2,5] (iD)

[1]College of Biology and the Environment, Joint Center for sustainable Forestry in Southern China, Nanjing Forestry University, Nanjing, China, [2]Yale-NUIST Center on Atmospheric Environment, International Joint Laboratory on Climate and Environment Change (ILCEC), Nanjing University of Information, Science and Technology, Nanjing, China, [3]Department of Soil, Water, and Climate, University of Minnesota, Twin Cities, St. Paul, MN, USA, [4]Ningbo Meteorological Observatory, Ningbo, China, [5]School of Forestry and Environmental Studies, Yale University, New Haven, CT, USA

Abstract Urban areas are global methane (CH$_4$) hotspots. Yet large uncertainties still remain for the CH$_4$ budget of these domains. The Yangtze River Delta (YRD), China, is one of the world's most densely populated regions where a large number of cities are located. To estimate anthropogenic CH$_4$ emissions in YRD, we conducted simultaneous atmospheric CH$_4$ and CO$_2$ mixing ratio measurements from June 2010 to April 2011. By combining these measurements with the Weather Research and Forecasting and Stochastic Time-Inverted Lagrangian Transport models and a priori Emission Database for Global Atmospheric Research emission inventories, we applied three "top-down" approaches to constrain anthropogenic CH$_4$ emissions. These three approaches included multiplicative scaling factors, flux ratio, and scale factor Bayesian inversion. The posteriori CH$_4$ flux density estimated from the three approaches showed high consistency and were 36.32 ($\pm$9.17), 35.66 ($\pm$2.92), and 36.03($\pm$14.25) nmol·m^{-2}·s^{-1}, respectively, for the duration of the study period (November 2010 to April 2011). The total annual anthropogenic CH$_4$ emission was 6.52($\pm$1.59) Tg for the YRD region based on the average of these three approaches. Our emission estimates were 30.2($\pm$17.6)%, 31.5 ($\pm$5.6)%, and 30.8 ($\pm$27.4)% lower than the a priori Emission Database for Global Atmospheric Research v432 emission inventory estimate. The scale factor Bayesian inversion results indicate that the overestimate was mainly caused by two source categories including fuel exploitation and agricultural soil emissions (rice cultivation). The posteriori flux densities for agricultural soil and fuel exploitation were 10.68 and 6.34 nmol·m^{-2}·s^{-1}, respectively, and were 47.8% and 29.2% lower than the a priori inventory. Agricultural soil was the largest source contribution and accounted for 29.6% of the YRD CH$_4$ budget during the study period.

1. Introduction

Atmospheric methane (CH$_4$) mixing ratios reflect the balance between CH$_4$ sinks and sources. Globally observed CH$_4$ mixing ratios showed a general stabilization between 1995 and 2006, with an increasing trend since 2007 (Kirschke et al., 2013; Nisbet et al., 2014). These trends suggest a large increase in anthropogenic CH$_4$ emissions or climate-induced natural emissions from global wetlands (Dlugokencky et al., 2009; Kirschke et al., 2013; IPCC 2013; Nisbet et al., 2016). There is considerable debate regarding the exact causal mechanisms, which highlights that CH$_4$ sources are still not fully understood and have relatively large uncertainties. Estimates of global CH$_4$ emissions vary considerably (542 to 852 Tg CH$_4$/year) with Intergovernmental Panel on Climate Change (IPCC)-based estimates generally much larger than that estimated from direct observations (or inversions) from atmospheric measurements (526 to 569 Tg CH$_4$/year; Kirschke et al., 2013; Nisbet et al., 2014, 2016, 2019). To better understand the global CH$_4$ cycle, CH$_4$ emissions at regional and subregional scales (10^2–10^6 km^2) need to be better monitored and constrained. Approximately 50% to 65% of CH$_4$ emissions come from anthropogenic sources such as fossil fuel exploitation (e.g., gas flaring and venting during coal mining, oil/gas production, and distribution losses by transmission), agricultural sector (e.g., agricultural soil (AGS), agricultural waste burning (AWB), enteric fermentation, and manure management), and landfills (waste), with fossil fuels and landfills accounting for about 52% of the total anthropogenic CH$_4$ emissions (IPCC 2013).

Urban areas are considered hotspots for greenhouse gas (GHG) emissions. Urban carbon dioxide (CO_2) emissions account for over 70% of fuel-related CO_2 emissions, and urban CH_4 emissions account for about 25% of global CH_4 emissions (IPCC 2013). Despite the disproportionate role that cities play in the global carbon cycle, large uncertainties persist at the regional to city scales (Mitchell et al., 2018; Wu et al., 2018). Improved knowledge of CH_4 emissions from urban areas is of high priority in improving our understanding of the global CH_4 cycle and for developing practical mitigation strategies (Hopkins et al., 2016; Townsend-Small et al., 2012; Wunch et al., 2016).

CH_4 mixing ratios are projected to increase substantially (6.9 ppb/year) assuming the same observed trend between 2007 and 2015 (Saunois et al., 2016). Most of this increase will be associated with anthropogenic emissions from developing countries (Duren & Miller, 2012). Based on high-resolution emission mapping, significant differences in GHG emissions between urban and rural areas have been identified and indicate that urbanization in developing countries are an important factor in driving increased GHG emissions (Wang et al., 2013). With the global urban population expected to double by 2050, CH_4 emissions are expected to undergo large increases in the absence of any mitigation strategies.

Due to increasing fossil fuel demand related to economic growth and residential needs, developing countries account for a large portion of this urbanization (Duren & Miller, 2012; International Energy Agency, 2008). Both economic growth and urbanization can potentially enhance CH_4 emissions from urban regions. China is the largest developing country in the world, with an actual economic growth rate of about 6% per year (Rosenzweig et al., 2010; Wolf et al., 2011). A recent study in China showed that the annual total anthropogenic CH_4 emission was 24.4 (18.6–30.5) Tg with the main contributions including rice cultivation (46%), livestock (25%), and coal exploitation (14%) for the year 1980. By 2010, these emissions had doubled to 44.9 (36.6–56.4) Tg with major changes in the relative contributions including coal exploitation (40%), livestock (25%), and rice cultivation (16%; Peng et al., 2016). To support urban carbon management strategies, robust verifications of anthropogenic emissions are needed and measurement systems are being deployed to monitor anthropogenic CH_4 emissions from representative megacities in China (Shen et al., 2014).

The Yangtze River Delta area (hereafter YRD) geographically includes Shanghai municipality, and the three provinces of Anhui, Zhejiang, and Jiangsu. It has a population of about 190 million and is ranked as one of the most developed and densest urbanized regions in the world (C. Hu, Liu, et al., 2018). The urban land fraction in YRD is greater than 10% and exceeds the global average of 2.4% (C. Hu, Liu, et al., 2018; Xu et al., 2017). As summarized for the year 2014, the YRD area accounted for 11% of the national population and 18.5% of China's gross domestic product (GDP; C. Hu, Liu, et al., 2018). Anhui province is among the highest coal mining CH_4-emitting provinces in China (Miller et al., 2019). The rice cultivation area in YRD also accounts for 18% of the total plant area in China (National Bureau of Statistics of China, 2010) and has potential to be a large CH_4 source. At the regional scale, the CH_4 emission sources from rural areas can also be a significant contributor to urban regions. For instance, the Four Corners region in the United States is dominated by fossil fuel emissions, while California's central Valley found that its CH_4 sources were dominated by agricultural emissions (Kort et al., 2014). Based on the IPCC methodology, previous research concluded that rice cultivation, coal mining, and landfills accounted for 42.1%, 26.4%, and 10.8%, respectively, of the total CH_4 emissions in YRD for 2009 (Shen et al., 2014). These results differ considerably compared to country-level emission estimates for China (Peng et al., 2016) and highlight the large variability and uncertainty in regional estimates. The YRD, therefore, represents a great opportunity for improving our understanding of urban GHG emissions and developing mitigation strategies.

Both bottom-up and top-down methods have been applied to estimate GHG emissions in China. Bottom-up approaches are typically based on the upscaling of inventory statistics and associated emission factors (EFs) obtained at relatively small spatial scales (i.e., chamber to field scales). Top-down approaches are typically based on atmospheric measurements and inverse modeling to constrain regional scale emissions (see details in Kirschke et al., 2013). Previous studies on anthropogenic CH_4 emissions have mostly been based on the IPCC bottom-up methodology. Peng et al. (2016) started an independent measurement-based survey of CH_4 emissions in China by using province-level EFs. They concluded that the national total emission was 44.9 Tg (range 36.6 to 56.4 Tg) in 2010. Their emission estimate is 36% lower than the Emission Database for Global Atmospheric Research (EDGAR42) inventory and 18% lower than that estimated by using the IPCC default EFs. By using Chinese economic data and the embodiment analysis, Zhang and Chen (2010)

reported that the total anthropogenic CH_4 emission was 39.6 Tg in 2007 for mainland China. Their analyses showed that agricultural and coal mining emissions were the most important sources, whereas emissions derived from EDGAR42 suggested a total emission of 73 Tg. These different studies highlight the large uncertainties that can propagate depending on the quality of the inventory and activity data (magnitude of activity and various carbon input and consumption processes that result in CH_4 emissions) when applying the IPCC approach.

There are large uncertainties associated with a number of source categories in China. A recent study estimated coal mining CH_4 EFs at the provincial level across China, which accounts for >50% of the global coal mining CH_4 emissions. Their study found that EFs are highly variable from 0.74 m^3/t (m^3 CH_4 per ton coal) to 36 m^3/t (Zhu et al., 2017). Methane emissions from landfills also have large uncertainties with projected emissions ranging from 1.80 to 2.35 Mt by 2030 (Cai et al., 2018). Aquaculture in China represents an important source of CH_4, accounting for 60% of the world total inland aquaculture area in 2012. Nearly half of China's aquaculture was converted from rice paddies to meet the demands of aquaculture production (Food and Agricultural Organization (FAO), 2014). Field experiments conducted in the YRD have shown that land use change can alter methane emissions. For instance, conversion from rice paddies to aquaculture caused methane emissions to increase by 48% in the YRD (Liu et al., 2016). Therefore, large biases can occur in bottom-up estimates without state-of-the-art land use information. Further, N. Hu et al. (2018) found that CH_4 emissions from natural gas vehicles were underestimated by eightfold in China by the IPCC inventory methodology. These studies indicate large biases for the IPCC default EFs for different regions and categories and also for the activity data used in calculating CH_4 emissions (N. Hu et al., 2018; Peng et al., 2016).

Top-down methods have already been widely used in estimating CH_4 emissions in other countries. These approaches include remote sensing and atmospheric measurement techniques and have shown great potential for retrieving and evaluating anthropogenic GHG emissions (Gurney et al., 2017; Hedelius et al., 2018; Miller et al., 2013; Pison et al., 2018). Based on the theory that "excess" GHG gas (i.e., enhancement) above "background" values can reflect the influence of both local emissions and meteorological conditions, top-down atmospheric techniques combine high-precision mixing ratio observations and transport modeling to constrain bottom-up emission estimates from urban regions (Mitchell et al., 2018; Salmon et al., 2018; Sargent et al., 2018). Townsend-Small et al. (2012) found that fugitive emissions of CH_4 in California, USA, were underestimated by more than ~50% based on isotopic constraints and the difference between their top-down estimates compared with with a priori inventories for California (Hopkins et al., 2016; Wong et al., 2015; Wunch et al., 2016). By applying a Bayesian inversion method, Chen et al. (2018) also reported that CH_4 emissions from oil/gas sources and livestock were underestimated by 1.3 and 1.8 times, respectively, for the Upper Midwestern United States. These results indicate that relatively large uncertainty still exist for anthropogenic CH_4 emissions at regional scales, which can be attributed to both uncertainties in activity data and EFs.

These top-down methods have rarely been applied in China and the YRD region. Thompson et al. (2015) employed the Bayesian inversion method to constrain CH_4 emissions in East Asia. They found that the total emissions for China were overestimated by the a priori estimations (EDGAR 42) by about 29% between 2000 and 2011. By combining aircraft observations of the Asian outflow (over the NW Pacific) with atmospheric transport modeling, Xiao et al. (2004) evaluated the model simulated concentration relationship of CH_4:CO with observations and concluded that a priori CH_4 emissions in east Asia should be increased by about 40% to match the observations. Jiang et al. (2014) constrained CO_2 fluxes in China by using aircraft CO_2 measurements, and their results reduced CO_2 flux uncertainty to 2–12%. Tohjima et al. (2014) argued that the atmospheric ΔCH_4: ΔCO_2 enhancement slope is equal to the emission ratio of CH_4 and CO_2 and found that annual anthropogenic CH_4 (excluding rice cultivation) emissions was 39 $\pm$ 7 Tg through 1998 to 2002. A recent study based on Greenhouse gases Observing SATellite observations was used to constrain CH_4 emissions in China. This study found that emissions showed an increasing trend over the period 2010 to 2015, with the emission magnitude around 20% smaller than that estimated from the EDGAR v4.3.1 inventory (Miller et al., 2019). Most of these previous top-down studies tried to constrain CH_4 emissions in China by using a single scaling factor (SF). However, as noted above, the uncertainties and SFs can vary dramatically for different regions (N. Hu et al., 2018; Peng et al., 2016). To the best of our knowledge, only Shen et al. (2014) have estimated CH_4 emissions within the YRD region. They used both the bottom-up IPCC

methodology and top-down approaches using the concentration ratio between CH_4 and CO_2 as a constraint. They concluded that CH_4 emissions from anthropogenic sources (excluding rice cultivation), rice cultivation, and natural wetland were 2.85($\pm$22%), 2.22 ($\pm$22%), and 0.19($\pm$20%) Gg in YRD for 2009. However, their work did not explicitly link the atmospheric measurements with concentration footprint modeling or Bayesian inversion methods to help constrain individual sources. The advantage of concentration source footprint modeling and Bayesian inversion source partitioning is the ability to provide constraints on a variety of source categories simultaneously.

The YRD region contains many strong anthropogenic CH_4 sources (Wang et al., 2009; Yan et al., 2003) including landfills, fossil-fuel related combustion, coal mining, and agricultural emissions. Quantifying GHG emissions for the region is needed to fill knowledge gaps related to GHG emissions and hotspots within the region. We conducted atmospheric concentration observations for both CH_4 and CO_2, where the CO_2 was used as a tracer to help constrain CH_4 emissions. The objectives of this study were, therefore, to (1) provide three top-down approaches to constrain anthropogenic CH_4 emissions for the YRD region, (2) reconcile the differences between bottom-up and top-down estimates of anthropogenic CH_4 emissions, and (3) identify the main CH_4 sources that contribute to these differences and provide insights on the development of future CH_4 mitigation strategies.

2. Materials and Methods

2.1. Mixing Ratio and Meteorological Observations

The atmospheric CH_4 and CO_2 mixing ratios reported in this study were measured at the Nanjing University of Information Science and Technology (NUIST, 32°12′N, 118°43′E) campus, which is located about 20 km north of Nanjing City, Jiangsu, China (Figure 1). There are no obvious point sources of CH_4 within 5 km of the NUIST site. The major CO_2 emission sources include the energy industry, manufacturing industry, and oil production/refineries located within a 100 km radius (C. Hu, Liu, et al., 2018). Our observations, therefore, can provide information related to emissions from ecosystems and point sources related to fugitive CH_4 emissions. The main sources of CH_4 include rice cultivation, fossil-fuel related combustion, fossil fuel exploitation, and landfill emissions. The measurements were conducted via a Yale-NUIST laboratory located on the ninth floor at a height of 34 m above ground. Atmospheric air samples were continuously pumped at a flow rate of 0.5 ml/s. Our previous studies conducted at the same site verified the observation height is representative of CH_4 and CO_2 mixing ratios within the YRD region (C. Hu, Liu, et al., 2018; Shen et al., 2014; Xu et al., 2017).

The observational record is defined by two periods. The first period includes simultaneous measurements of CH_4 and CO_2 mixing ratios from June 2010 to April 2011 using an infrared gas analyzer (model G1301, Picarro Inc., Sunnyvale, California, USA). Measurement precision for CH_4 was 0.7 and 50 ppb for CO_2, respectively, based on 5-min averages. Span calibrations (3,050 ppb for CH_4 and 390 ppm for CO_2) indicated that the uncertainty was within 1% over the course of the experimental period (Shen et al., 2014). The second period included continuous observations for 3 years from March 2013 to August 2015. Here, only CO_2 mixing ratios were measured using an infrared gas analyzer (model G1101-I, Picarro Inc., Sunnyvale, California, USA). The CO_2 mixing ratios were calibrated every 3 hr against standards traceable to the National Oceanic and Atmospheric Administration (NOAA), Earth System Research Laboratory. Based on the Allan variance analysis, the precision of the hourly measured CO_2 mixing ratio was 0.07 ppm. Detailed information regarding the site description and calibration strategies are provided in Shen et al. (2014) and Xu et al. (2017).

To reduce the effects of natural biological sources on our CH_4 inversion, we defined a cold/dormant period (winter and early spring, November 2010 to April 2011) in order to better constrain the anthropogenic emissions. A similar methodology was performed by Tohjima et al. (2014) who constrained anthropogenic CH_4 emissions for Asia. Wetland CH_4 emissions are typically 50 to 300 $\mu g \cdot m^{-2} \cdot hr^{-1}$ in winter and spring and 6,000 to 15,000 $\mu g \cdot m^{-2} \cdot hr^{-1}$ in summer for the YRD region (Wang et al., 2009). When considering wetland and fuel combustion emissions through the whole year, winter emissions represent less than 1% of the total CH_4 emissions (Shen et al., 2014). Natural emissions, therefore, are likely to be negligible when compared with the average anthropogenic CH_4 emissions during winter.
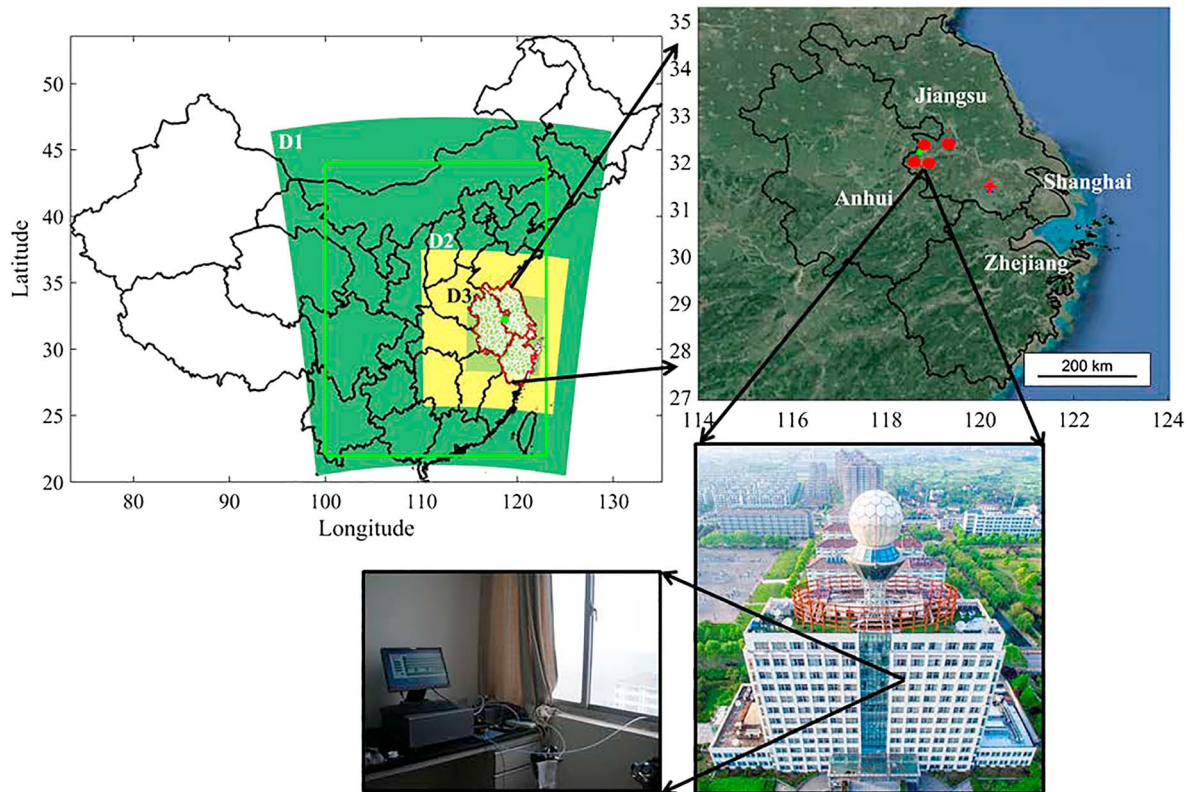
Figure 1. Simulation domains used in the Weather Research and Forecasting-Stochastic Time-Inverted Lagrangian Transport model with view of Nanjing University of Information Science and Technology site for CH_4/CO_2 observations (green dot), radiation site (red "x"), and other meteorological evaluation sites (red dots).

Meteorological variables including 10-m wind speed (U_{10m}), 2-m air temperature (T_{2m}), relative humidity (RH), downward shortwave (DSWR), and downward longwave radiation (DLWR) were chosen to evaluate the performance of the Weather Research and Forecasting (WRF) model for the YRD. Four meteorological sites, Liuhe, Pukou, Nanjing, and Yangzhou located in four different directions from the NUIST observation site were selected (red dots, Figure 1). These four sites are from the surface stations of the Chinese National Meteorological Center (http://cdc.cma.gov.cn/). All of the site information is listed in Table 1. The MLW site provides the radiation observations (red "x" in Figure 1) and have been reported in detail by Lee et al. (2014). U_{10m}, DSWR, and DLWR are hourly observations, and T_{2m} and RH are measured at 02:00, 08:00, 14:00, and 18:00 (local time). Evaluation metrics of mean bias and root-mean-square error (RMSE) for these meteorological variables are summarized in section 3.1 and Table 3.

2.2. WRF-STILT Model Setup and Simulation of CH_4/CO_2 Mixing Ratios

The Stochastic Time-Inverted Lagrangian Transport (STILT) model is a receptor-oriented model and has been widely applied in the transport simulation of many trace gases including CH_4 (Chen et al., 2018; Verhulst et al., 2017), CO_2 (Graven et al., 2018; C. Hu, Griffis, et al., 2018; C. Hu, Liu, et al., 2018), N_2O (Chen et al., 2016; Griffis et al., 2017), and CO (Kim et al., 2013). The STILT model can accurately simulate the source footprint (influence-weighting functions) for a given receptor. The footprint indicates the sensitivity of the observation taken from a particular location and sample height to different emission sources. By using the STILT model framework the mixing ratio enhancements can be derived by multiplying the footprint function with emission maps (Gerbig et al., 2003; Lin, 2003).

The footprints were simulated by releasing a large number of particles from the receptor and tracing their locations backward for every two integration minutes. The backward transport of these particles was driven by high-resolution meteorological fields and boundary layer conditions (e.g.,3-D wind fields, potential temperature, RH, air density, surface roughness length, and friction velocity; Nehrkorn et al., 2010). By keeping

Table 1
Mixing Ratio and Meteorological Sites Information

Site	Latitude	Longitude	Direction of NUIST site	Observed variables	Period
NUIST	32°12′	118°43′		CO_2 and CH_4 mixing ratio	June 2010 to April 2011 (CO_2/CH_4), March 2013 to August 2015 (CO_2)
Nanjing	31°56′	118°54′	South	Wind speed, air temperature, relative humidity	December 2010 to April 2011
Liuhe	32°22′	118°51′	North	Wind speed, air temperature, relative humidity	December 2010 to April 2011
Pukou	32°03′	118°37′	West	Wind speed, air temperature, relative humidity	December 2010 to April 2011
Yangzhou	32°25′	119°25′	East	Wind speed, air temperature, relative humidity	December 2010 to April 2011
MLW	31°25′	120°13′		Downward longwave radiation, downward shortwave radiation	December 2010 to April 2011

Note. NUIST = Nanjing University of Information Science and Technology; MLW = Mei Liang Wan.

track of how long each of these particles resides in a given horizontal and vertical grid box, the footprint is then calculated by integrating the residence time of these particles in the planetary boundary layer as described in Lin et al. (2003).

The main parameters in the STILT model setup include number of released particles, back trajectory time, and location and height of the receptor. Following the setup used in our previous work (Chen et al., 2018; Griffis et al., 2017; C. Hu, Griffis, et al., 2018), 500 particles were released per hour from the same location of our CH_4/CO_2 observation site (34-m height, 32°12′N, 118°43′E). These particles were then tracked backwards in time for 7 days. In most cases this was sufficient time for the particles to reach the boundary of the outermost domain (green rectangle in Figure 1). We used WRF (version 3.5.1) to simulate the meteorological fields used to drive the STILT model. Three domains with spatial resolution of 27, 9, and 3 km were used. Here, the innermost domain included the whole YRD (Table 2). The same PBL and microphysical options were applied by C. Hu, Liu, et al. (2018) to study CO_2 emissions within the same region. Their study showed that the model had satisfactory performance in simulating the near-surface air temperature, DSWR, wind direction, and wind speed for the YRD.

The CH_4 and CO_2 mixing ratios were simulated as the sum of the enhancement and background mixing ratios as in equations (1) and (2):

$$(CH_4)_{model} = (CH_4)_{background} + (\Delta CH_4)_{enhancement} \tag{1}$$

$$(\Delta CH_4)_{enhancement} = \sum_{i=1}^{168} \sum_{j=1}^{n} \left[footprint_{i,j} \times flux_{i,j} \right] \tag{2}$$

These equations are expressed for CH_4. Identical equations can be written for CO_2 (i.e., replace CH_4 with CO_2 in equations (1) and (2)). The enhancement term, $(\Delta CH_4)_{enhancement}$, is the cumulative hourly contributions for the past 168 hr for different source categories. $footprint_{i,j}$ is the footprint in each grid cell (j) for each hour (i), and $flux_{i,j}$ is the flux corresponding to the same grid cell and hour. The background mixing ratio, $(CO_2)_{background}$, was calculated following the method of C. Hu, Liu, et al. (2018) and C. Hu, Griffis, et al. (2018). They tracked the air flow of released particles to the outermost boundary, and the CO_2 background fields were obtained from CarbonTracker (section 2.3). At the present time a similar global CH_4 data

Table 2
WRF Model Domains Setup

Domain setup	Domain 1	Domain 2	Domain 3
Study area	Central and east China	East China	Yangtze River Delta area
Spatial resolution	27 km	9 km	3 km
East-west grid numbers	105	154	253
South-north grid numbers	111	148	223

Note. WRF = Weather Research and Forecasting.

product like CarbonTracker is not available. Therefore, we defined the background CH_4 mixing ratio, $(CH_4)_{background}$, as the average of two NOAA CH_4 background sites based on the NOAA global network including Waliguan (WLG) and Ulaan Uul Mongolia (UUM) (more details in section 2.3), which are located to the north (UUM 1020 km) and northwest (WLG 1700 km) of the NUIST site. To derive hourly adjusted CO_2 anthropogenic emissions for different categories, we used the CO_2 emission SFs from Vulcan (Gurney et al., 2009; C. Hu, Liu, et al., 2018).

2.3. A Priori CH₄ and CO₂ Flux and Background Data

A number of emission inventories are available for CO_2 and CH_4 including the U.S. Environmental Protection Agency (https://www.epa.gov/), VULCAN (Gurney et al., 2009), the Fossil Fuel Data Assimilation System (Rayner et al., 2010), Open-source Data Inventory for Anthropogenic CO_2 (Oda & Maksyutov, 2016), and EDGAR products. The Fossil Fuel Data Assimilation System, Open-source Data Inventory for Anthropogenic CO_2, and EDGAR cover the global scale. while the U.S. Environmental Protection Agency and VULCAN are specific to the United States. The EDGAR products have been widely used in evaluating GHG inventories (C. Hu, Griffis, et al., 2018; Peng et al., 2016; Thompson et al., 2015) given their comprehensive and relatively detailed subcategories. The EDGAR products are used here as the a priori flux estimates to constrain both the anthropogenic CH_4 and CO_2 calculations. EDGAR v432 and EDGAR v42 have the same fine spatial resolution of $0.1° \times 0.1°$. However, EDGAR v42 emissions represent annual values whereas EDGAR v432 vary monthly (Figures 2a–2d). Based on the EDGAR v432 monthly CH_4 inventories, the total anthropogenic CH_4 flux densities were 47.4 nmol·m^{-2}·s^{-1} for 2010 and 52.1 nmol·m^{-2}·s^{-1} for YRD from November to April 2011. The CH_4 emission in March was almost 2 times the monthly emission from November to January, which was contributed by rapidly increased CH_4 emissions from AGS (rice cultivation). This indicates that relatively large variations exist for different months. Consequently, we used EDGAR v432 as the a priori emissions to help represent the temporal variability within the inversion framework and also applied EDGAR v42 for comparison with EDGAR v432.

In EDGAR v432 anthropogenic CH_4 emissions are separated into 21 subcategories including AGS, AWB, enteric fermentation, and manure management, fuel exploitation (PRO), energy for buildings (RCO), oil refineries and transformation industry (REF), waste water handling (WWT), solid waste landfilling, and road transportation. We note that in EDGAR v432, rice cultivation is the only contributor to AGS emissions. Based on our inventory analyses for the YRD region in 2010, emissions from AGS accounted for the largest proportion of anthropogenic CH_4 emissions. During our study period (November to April), emissions from PRO, WWT, RCO, and REF show less seasonal variations between cold/dormant period and the whole year (see details in section 3.2). The monthly CH_4 emissions for the main sources in the YRD area are displayed in Supporting Information Figure S1.

In EDGAR v432 the CO_2 emissions are separated into two broad categories of short-cycle biofuel CO_2 emissions (nine subcategories, i.e., combustion of biofuel and AWB) and fossil fuels (20 subcategories). The CO_2 emission from fossil fuels for the YRD region was 3.66 and 0.30 μmol·m^{-2}·s^{-1} for short-cycle emissions in the year of 2010, indicating that fossil fuel combustion accounted for 93% of the total CO_2 emissions. To calculate the CO_2 enhancement from ecosystem respiration and photosynthesis, we used the net ecosystem CO_2 exchange CarbonTracker product. This product is based on the optimization of the CASA model via a CO_2 inversion using global observations (Peters et al., 2007). As shown in Figure 2e, net ecosystem CO_2 exchange was relatively small for the YRD when compared with anthropogenic CO_2 emissions in our study period (November 2010 to April 2011)..

The CO_2 background concentration data are from the CarbonTracker global CO_2 distributions (spatial resolution of $3° \times 2°$ and 3-hourly intervals), which was simulated using the TM5 transport model with optimized CO_2 flux (Peters et al., 2007). Since CH_4 mixing ratio distributions are not available for China during our study period, we followed the strategy of Chen et al. (2018) and selected NOAA flask sites as background values (Chen et al., 2018; Dlugokencky et al., 2009). Since the prevailing winds during winter are from north China, we selected flask sites WLG (36°17′N, 100°54′E, 3,810-m height) and UUM (44°27′N, 111°01′E, 1,007-m height) to define the background CH_4 mixing ratio (https://www.esrl.noaa.gov/gmd/dv/data/). Here, we linearly interpolated the weekly sampled CH_4 mixing ratios to hourly values. Averages of these two sites were used as hourly CH_4 background fields. The CCGCRV (a digital filtering
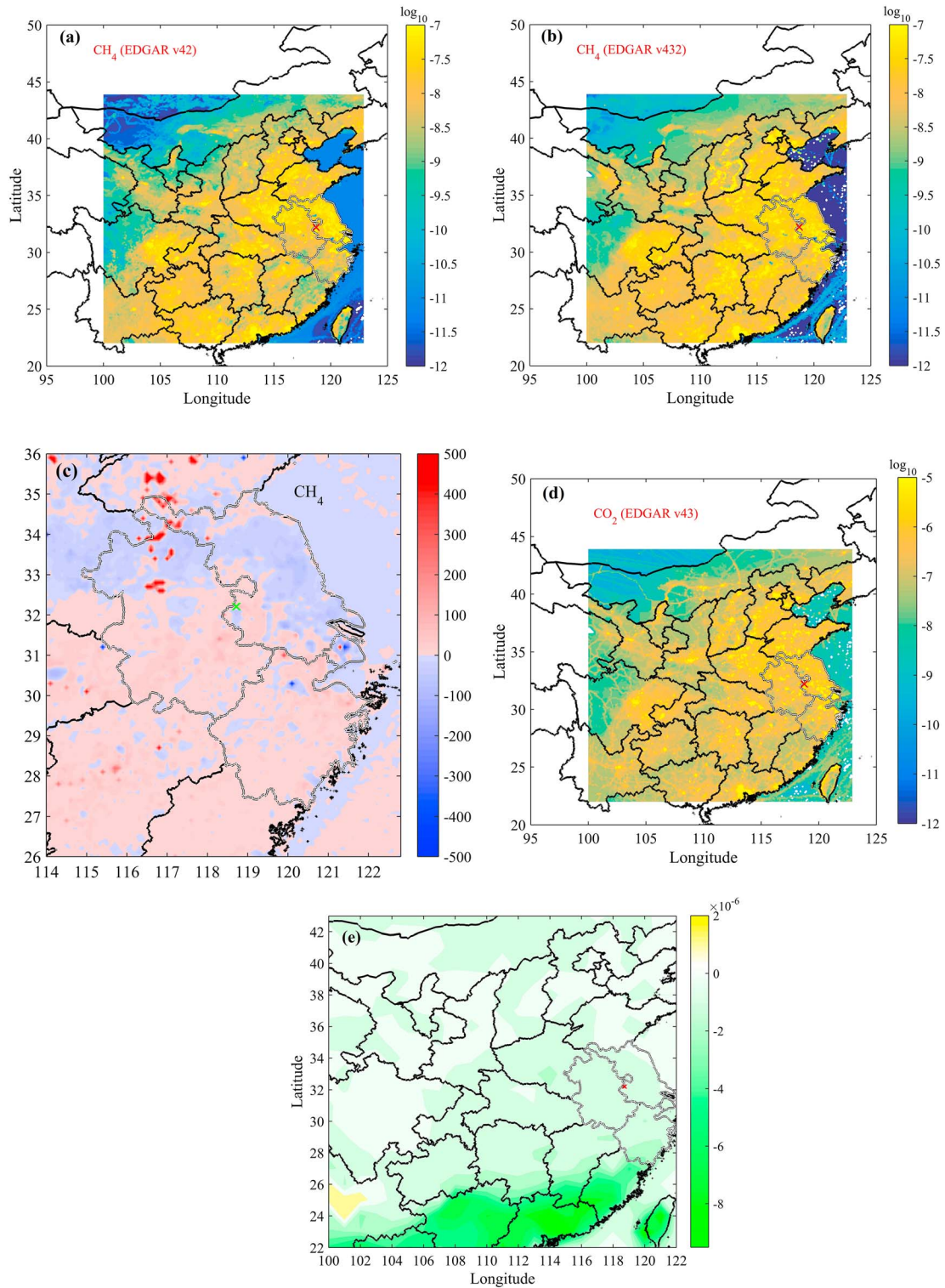
Figure 2. (a) Anthropogenic CH_4 emissions from EDGAR v42, units: $\log_{10}(\mathrm{mol \cdot m^{-2} \cdot s^{-1}})$, (b) EDGAR v432, units: $\log_{10}(\mathrm{mol \cdot m^{-2} \cdot s^{-1}})$, and (c) the difference between EDGAR v432 and EDGAR v42, units: $\mathrm{nmol \cdot m^{-2} \cdot s^{-1}}$, and (d) anthropogenic CO_2 emissions from EDGAR v432, units: $\log_{10}(\mathrm{mol \cdot m^{-2} \cdot s^{-1}})$, and (e) biological CO_2 flux from CarbonTracker, units: $\mathrm{mol \cdot m^{-2} \cdot s^{-1}}$. EDGAR = Emission Database for Global Atmospheric Research.

curving fitting program developed by Carbon Cycle Group, NOAA, USA) regression method has also been recommended for fitting flask observations (Thoning et al., 1989), the comparison between linear interpolation and CCGCRV regression produced very similar results (section 3.3). Further, by applying the observed linear relationship between CO_2 and CH_4, the CH_4 background value can be approximated from the CO_2 background data (Wang et al., 2010). Given that the background CO_2 mixing ratio in winter was 395 ppm we estimated a background CH_4 mixing ratio of about 1,860 ppb (see details in section 3.5).

2.4. Constraining CH_4 emissions

Three different approaches were used to constrain the anthropogenic CH_4 emissions for the YRD region including (1) multiplicative scaling factors (MSF), (2) flux ratios (FR), and (3) scale factor Bayesian inversion (SFBI). Figure 3 provides an overview of the strategy used. The key steps included (1) simulating CH_4 and CO_2 enhancements by multiplying the source footprints with the a priori emission maps, (2) applying the MSF method to constrain the a priori CH_4 and CO_2 emissions, (3) using the calibrated CO_2 emissions with the FR approach to constrain CH_4 emissions, (4) applying the SFBI approach to constrain the total and partitioned CH_4 emissions, and (5) comparing the results from these three different methods to assess the consistency of the posteriori anthropogenic CH_4 emissions for the YRD region.

2.4.1. MSF Approach

The accumulation of GHG mixing ratios in urban domes has been identified as a suitable approach for retrieving urban emissions. This is based on the theory that an air mass records the enhancement of atmospheric CH_4 and CO_2 mixing ratios. Such enhancements represents excess mixing ratios that can be used to quantify GHG emissions (Duren & Miller, 2012; Miller et al., 2013). The MSF approach has been used in many urban areas such as Nanjing, China (C. Hu, Liu, et al., 2018) and Boston, USA, (Sargent et al., 2018). The SFs can be derived by dividing the observed GHG enhancements by the modeled GHG enhancements. Here, this approach consists of two main steps: (1) The observed GHG enhancements were estimated from the observations by subtracting the sum of background data and the biological enhancements (C. Hu, Liu, et al., 2018; Sargent et al., 2018). The modeled GHG enhancements were obtained by multiplying the source footprints with the anthropogenic emissions; and (2) to reduce the random errors of the modeled hourly enhancements, the SFs were derived by using monthly averages of these values. Therefore, the SFs for CH_4 and CO_2 were calculated as

$$SF_{CH_4} = \frac{Obs_{CH_4} - CH_{4background}}{\Delta CH_{4Anthro\_enhancement}} \tag{3}$$

$$SF_{CO_2} = \frac{Obs_{CO_2} - CO_{2background} - \Delta CO_{2Bio\_enhancement}}{\Delta CO_{2Anthro\_enhancement}} \tag{4}$$

where *Obs* is observed atmospheric mixing ratio, and Δ indicates simulated enhancement of corresponding source categories related to biological (subscript Bio_enhancement) and anthropogenic (subscript Anthro_enhancement) fluxes. Note that the CO_2 emissions are constrained here so that it can be used as a tracer to retrieve CH_4 emissions using the FR method (described below).

The MSF approach is susceptible to errors in the background mixing ratio estimate, the WRF simulated meteorological fields, and the STILT back trajectories. Following the strategy of C. Hu, Liu, et al. (2018), we used a Monte Carlo approach (applied to equations (3) and (4)) to assess the extent to which these factors impacted the results. Here, we assumed a normal sample distribution with the lower 2.5% and upper 97.5% of the values considered as the uncertainty (Cao et al., 2016). We assigned relative uncertainties for the Monte Carlo simulations as follows: The uncertainty associated with the meteorological fields and particle back trajectories was assigned a mean value of 13% based on previous studies (Chen et al., 2018; Guo et al., 2016; C. Hu, Liu, et al., 2018). A much larger uncertainty of 50% was assigned to the biological CO_2 enhancement (Peters et al., 2007). A 1% uncertainty was assigned to the observed CO_2 and CH_4 mixing ratios based on the quality of span calibrations (Shen et al., 2014). The uncertainty in the background CO_2 mixing ratio was assigned a value of 0.5% based on our analysis of Mauna Loa observations versus the Carbon Tracker estimate for the same location. For instance, results for the whole year showed a mean bias of 0.18 ppm (0.05%), standard deviation of 0.60 ppm (0.16%) compared with the mean annual observation of
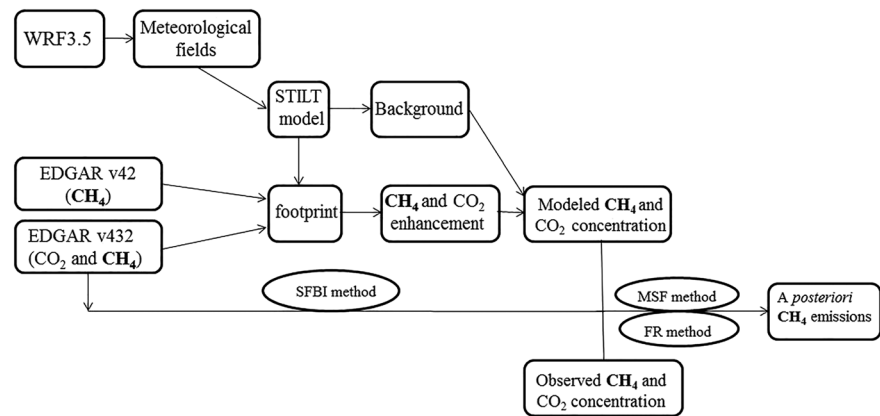
Figure 3. Overview of the three different top-down methods for constraining CH_4 emissions in the Yangtze River Delta region, China. EDGAR = Emission Database for Global Atmospheric Research; FR = flux ratio; MSF = multiplicative scaling factors; SFBI = scale factor Bayesian inversion; STILT = Stochastic Time-Inverted Lagrangian Transport; WRF = Weather Research and Forecasting.

385 ppm for 2008. The uncertainty in the CH_4 background values was determined as the relative average difference between the two NOAA sites (2%).

2.4.2. FR Approach

The FR approach has been widely applied to derive emissions of target gases that are difficult to measure (Shen et al., 2014; Turnbull et al., 2011; Vardag et al., 2015; Wang et al., 2013). This approach is based on the assumption that the two different gases are well mixed, with no significant chemical losses during the transport process, and that their concentration regression slope is representative of the emission ratio. Based on our previous work, we have shown that CO_2 emissions are well constrained and have less uncertainty when compared to CH_4 for YRD (C. Hu, Liu, et al., 2018; Shen et al., 2014; Xu et al., 2017).

Here we use CO_2 as a tracer to help constrain CH_4 emissions for the YRD region. The FR was calculated using equations (5)–(8):

$$O_{slope} = \frac{O_{emissionCH_4}}{O_{emissionCO_2}} \tag{5}$$

$$M_{slope} = \frac{M_{emissionCH_4}}{M_{emissionCO_2}} \tag{6}$$

$$O_{CH_4} = \frac{M_{CH_4}}{\frac{M_{slope}}{O_{slope}}} \times \frac{O_{CO_2}}{M_{CO_2}} = \frac{M_{CH_4}}{SF}, \left(SF = \frac{\frac{M_{slope}}{O_{slope}}}{\frac{O_{CO_2}}{M_{CO_2}}} \right) \tag{7}$$

$$posteriori\_YRD_{CH_4} = \frac{priori\_YRD_{CH_4}}{SF} \tag{8}$$

where O_{slope} is observed regression slope for atmospheric CH_4 ($O_{atmosphericCH_4}$) and CO_2 ($O_{atmosphericCO_2}$) observations. $O_{emissionCH_4}$ and $O_{emissionCO_2}$ represent the correct emissions of CH_4 and CO_2. M_{slope} is regression slope for modeled atmospheric CH_4 ($M_{atmosphericCH_4}$) and CO_2 concentration ($M_{atmosphericCO_2}$) obtained from the a priori emissions. $M_{emissionCH_4}$ and $M_{emissionCO_2}$ represent the a priori emissions for CH_4 and CO_2. MSF is the derived SF of CH_4 for different footprint source areas, and $\frac{O_{CO_2}}{M_{CO_2}}$ is a SF for CO_2 that was derived previously from the MSF methodology. The $priori\,YRD_{CH_4}$ is the a priori CH_4 emission for YRD, and $posteriori\,YRD_{CH_4}$ is the optimized CH_4 emissions for YRD.

We calculated the emission ratios between CH_4 and CO_2 with different areas radius and found that the emission ratios are 0.032 ± 0.005 as the source area radius increased from 50 to 500 km, and more details are shown in Figure S2. This uncertainty was driven by the heterogeneous distribution of both CO_2 and CH_4 in YRD and this variability represents the relative uncertainty in the FR approach for the region.

2.4.3. SFBI Approach

In the SFBI approach the optimal solution is to minimize the cost function $J(\Gamma)$, which represents the mismatch between measured and simulated CH_4 concentrations and the mismatch between the a priori and posteriori SFs. Both of these are weighted by the corresponding error terms. The cost function $J(\Gamma)$ has the form

$$2J(\Gamma) = (y - K\Gamma)^T S_e^{-1} (y - K\Gamma) + (\Gamma - \Gamma_a)^T S_a^{-1} (\Gamma - \Gamma_a) \tag{9}$$

where y represents the observed CH_4 concentrations after subtracting the background CH_4 value, K is the Jacobian matrix whose values represent sensitivities of observations to the corresponding source contributions, Γ includes the a posteriori SFs for the various source contributions, S_e and S_a are the error covariance matrices for observations and the a priori values. Here Γ_a is treated as 1. Therefore, the solution for minimizing this cost function and obtaining the posteriori SFs is to solve $\nabla_\Gamma J(\Gamma) = 0$, as

$$\Gamma_{post} = \left(K^T S_e^{-1} K + S_a^{-1}\right)^{-1} \left(K^T S_e^{-1} y + S_a^{-1} \Gamma_a\right) \tag{10}$$

The SFBI method requires the construction of error covariance matrices and a state vector for the a priori and observational data. Two primary model errors arise from both WRF model simulated boundary layer height (S_{PBLH}) and the number of particles released in the STILT model ($S_{particles}$). Following previous work, we assigned an uncertainty value of 13% for relative bias in $S_{particles}$ in STILT (Chen et al., 2018; C. Hu, Liu, et al., 2018; Kim et al., 2013). Given the lack of boundary layer height observations, a 10% uncertainty was assigned to S_{PBLH} based on previous work in China (Guo et al., 2016). We assigned an uncertainty of 100% for the a priori sources including AGS, PRO, RCO, REF, WWT, and Others (i.e., the sum of all remaining categories) following previous studies (Peng et al., 2016; Shen et al., 2014; Thompson et al., 2015; Tohjima et al., 2014).

We applied two strategies to obtain the uncertainty in the background, observed, and simulated CH_4 mixing ratios. The first strategy (hereafter strategy 1) assumed the observed CH_4 enhancements as y (true values, described in section 2.4.1) and the WRF-STILT simulated CH_4 enhancements as tagged tracer mixing ratios from each of the main sources being optimized. Here the observed CH_4 enhancements represent observations minus the background mixing ratios. Both contain uncertainties related to the analyzer measurement noise. In this strategy a value of 0.7 ppb was used as reported in a previous study (Shen et al., 2014). As described above, the uncertainty in the background CH_4 value ranged from about 2% to 5%. Therefore, we conservatively estimated the uncertainty in S_{obs} as $0.7 + 0.05 \times \text{obs}$. In the second strategy (hereafter strategy 2) we estimated the uncertainty in observations and background CH_4 separately. Here, we defined the observed CH_4 mixing ratio observations as y and treated the background CH_4 as a variable in x to be optimized together with the other six categories (defined above). In this case we assigned a higher uncertainty value for the background as 10% and the uncertainty of CH_4 mixing ratio observations calculated as $0.7 + 0.002 \times \text{obs}$.

3. Results

3.1. Evaluation of Model Meteorological Fields for YRD

The quality of the WRF model simulated meteorological fields has been evaluated using multiple observations throughout the YRD region. The model simulated reasonably well the T_{2m}, U_{10m}, RH, DLWR, and the DSWR for the whole study period (Table 3). As shown in Figure S3, simulated meteorological variables showed excellent agreement with the observations, capturing the diel, daily, and seasonal patterns. The DLWR was slightly underestimated and the DSWR was slightly overestimated (DLWR: RMSE = 46.78 W/m^2, $r = 0.81$, DSWR: RMSE = 155.86 W/m^2, $r = 0.87$). These biases can be explained by the systematic underestimation of simulated clouds by WRF (Zhao et al., 2013).

3.2. WRF-STILT Simulated Footprints and EDGAR Inventory

The hourly concentration footprints from the study period (November 2010 to April 2011) were averaged and are displayed in Figure 4a. The monthly average concentration footprints are also shown in Figure S4. Previous studies have defined the most sensitive zone as the source areas with a footprint smaller

Table 3
Performance Statistics for Meteorological Fields at Four Selected Sites: Liuhe, Pukou, Nanjing, and Yangzhou, China, From December 2010 to April 2011

	Liuhe			Pukou			Nanjing			Yangzhou		
	RMSE	r	MB	RMSE	r	MB	RMSE	r	MB	RMSE	r	MB
U_{10m} (m/s)	2.17	0.61	1.38	2.34	0.60	2	1.98	0.58	0.85	2.84	0.45	2.07
RH (%)	18.26	0.71	6.2	16.88	0.71	4	17.1	0.74	5.34	16.44	0.71	2.21
T_{2m} (°C)	3.27	0.95	2.09	3.39	0.94	2	3.55	0.94	2.49	3.68	0.93	2.43

Note. Mean bias (MB) and root-mean-square error (RMSE) are displayed. RH = relative humidity; T_{2m} = 2-m air temperature; U_{10m} = 10-m wind speed.

than 10^{-4} ppm m^2 s/µmol (Chen et al., 2016, 2018; Kim et al., 2013). C. Hu, Liu, et al. (2018) and C. Hu, Griffis, et al. (2018) quantified a threshold of 10^{-3} ppm m^2 s/µmol as the intense source area defined where 80% of the CO_2 enhancement was realized. We used a similar approach to define the most intense source area for CH_4 emissions. As shown in Figure 4a, the intense source area (yellow shading) includes east Anhui and west Jiangsu Province. This region accounted for 84% of the total anthropogenic CH_4 enhancement. When applying a threshold of 10^{-4} ppm m^2 s/µmol, we observed that 97% of the CH_4 enhancement had a source from within the greater YRD region. Given the footprint pattern for each month we see a northwest-southeast orientation (November to March), controlled by the northeast monsoon in winter. Further, these source footprints indicate that the selected background NOAA CH_4 sites in the north are suitable for these inverse analyses.

3.3. Comparison Between Observations and Modeled CH_4 and CO_2 Mixing Ratios

EDGAR v432 was used to estimate the anthropogenic CO_2 emissions and EDGAR v42 and EDGAR v432 were used to simulate the CH_4 mixing ratios to provide a robust comparison. Based on the inventory analyses for the YRD region in 2010, emissions from AGS averaged 18.17 nmol·m^{-2}·s^{-1} and accounted for the largest proportion (38.4%) of anthropogenic CH_4 emissions. The remainder of the anthropogenic CH_4 emissions were dominated by PRO (8.87 nmol·m^{-2}·s^{-1}, 18.7%), WWT (7.57 nmol·m^{-2}·s^{-1}, 16.0%), RCO (3.91 nmol·m^{-2}·s^{-1}, 8.3%), and REF (0.92 nmol·m^{-2}·s^{-1}, 2.0%). During our study period (November to April), emissions from AGS averaged 20.46 nmol·m^{-2}·s^{-1} (39.3%), PRO (8.95 nmol·m^{-2}·s^{-1}, 17.2%), WWT (7.63 nmol·m^{-2}·s^{-1}, 14.7%), RCO (5.60 nmol·m^{-2}·s^{-1}, 10.8%), and REF (0.92 nmol·m^{-2}·s^{-1}, 1.8%). They show less variation between the cold/dormant period and the whole year. The monthly CH_4 emissions for the main sources are displayed in Figure S1. These emissions are also compared to those derived from the linear interpolation and CCGCRV regressions (Figure S5). Here, the estimated emissions are in excellent agreement and differ by less than 0.5%. Therefore, we present the remaining results based on the simple linear interpolation method. As shown for CO_2 in Figures 5a and 5b, the simulated CO_2 mixing ratios using
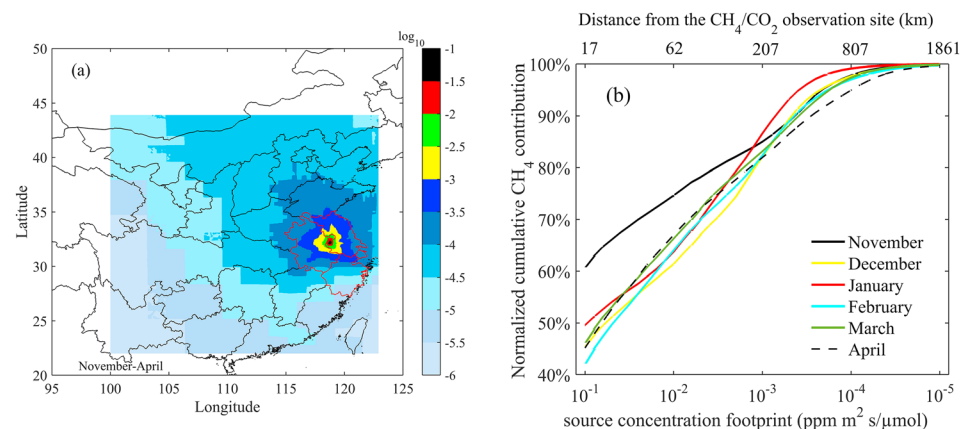

Figure 4. Averaged concentration footprints (ppm m^2 s/µmol) from November 2010 to April 2011 (a), and normalized CH_4 contribution from different source footprint sizes (b).
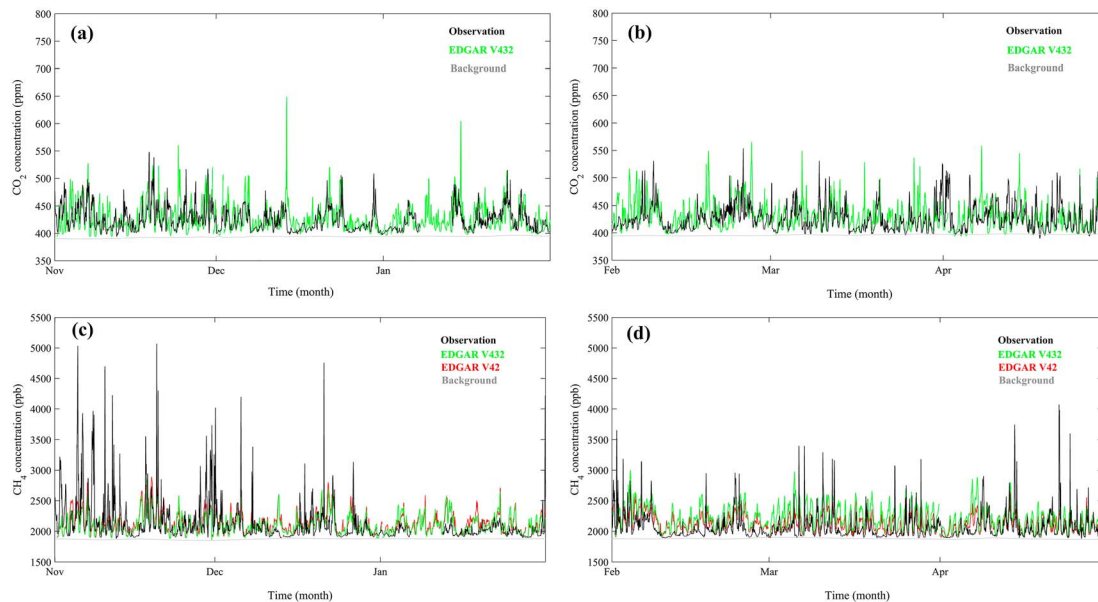
Figure 5. Comparison between observed and modeled hourly CO_2 from (a) November to January, (b) February to April, and CH_4 mixing ratios from (c) November to January, (d) February to April.

EDGAR v432 captured the diel and daily patterns of the observations reasonably well, yielding a correlation coefficient $R^2 = 0.12$ ($n = 4178$, $P < 0.001$) and RMSE = 23.4 ppm. This indicates relatively good performance for both the WRF simulated meteorological fields and the simulation of the particle back trajectories using the STILT model. The high consistency with the CO_2 observations also revealed less bias for the EDGAR v432 versus the EDGAR v42 inventories of anthropogenic CO_2 emissions.

According to the Yale-NUIST laboratory observations the mean CH_4 mixing ratio was 2,089.2 ppb during November 2010 to April 2011. The measured CH_4 mixing ratios at the background site Lin'An (119.44°E, 30.18°N, located in Zhejiang province, YRD) were 1,935, 1,947, and 1,961 ppb for the years 2009, 2010, and 2011, respectively (Fang et al., 2013). These CH_4 mixing ratios at Lin'An background site are still higher when compared with NOAA background sites at UUM and WLG (1,874.6 ppb on average), and indicate contribution by regional anthropogenic CH_4 signals. The difference between our measured value at Yale-NUIST and the Lin'An site reflects the strong anthropogenic CH_4 enhancements that occurred in YRD. Examination of the hourly observations for different months indicates a number of emission peaks and hot moments. These mainly occurred in November and December. The CO_2 observations during the same period did not show the same hot moments indicating that CO_2 and CH_4 are not always coemitted from the same sources during these periods. The CH_4 hot moments were likely driven by emissions from WWT and solid waste landfilling, which will be discussed later. In general, the simulated mixing ratios with both inventories captured the diel and daily patterns of observations reasonably well with $R^2 = 0.18$ ($n = 4221$, $P < 0.001$) and RMSE = 237.1 ppb for v432, and $R^2 = 0.15$ ($n = 4221$, $P < 0.001$) with RMSE = 225.5 ppb for v42, respectively. The model results were generally biased high for most of the study period for both of these two CH_4 inventories (77.1 ppb for v432 and 41.7 ppb for v43), especially from January to April, indicating that the bottom-up inventories overestimated the CH_4 emissions.

Averaged diel variations of CO_2 and CH_4 from November 2010 to April 2011 are shown in Figure 6. The simulated CO_2 and CH_4 mixing ratios showed similar diel patterns with peaks at 08:00 to 09:00 local time and then gradually decreasing to minimum values around 18:00. The modeled diel variations for CO_2 were in very good agreement with the observations, with $R^2 = 0.64$ ($P < 0.001$), RMSE = 8.8 ppm for the averaged diel patterns for these 6 months. However, the observed CH_4 mixing ratios were always lower compared to the modeled results for the period December to April, with November being an exception. Here, the $R^2 = 0.71$ ($P < 0.001$) and RMSE = 90.9 ppb for v432 and the $R^2 = 0.73$ ($P < 0.001$) and RMSE = 76.5 ppb for v42 for the diel patterns for these 6 months. As noted above, the underestimation of the CH_4 mixing
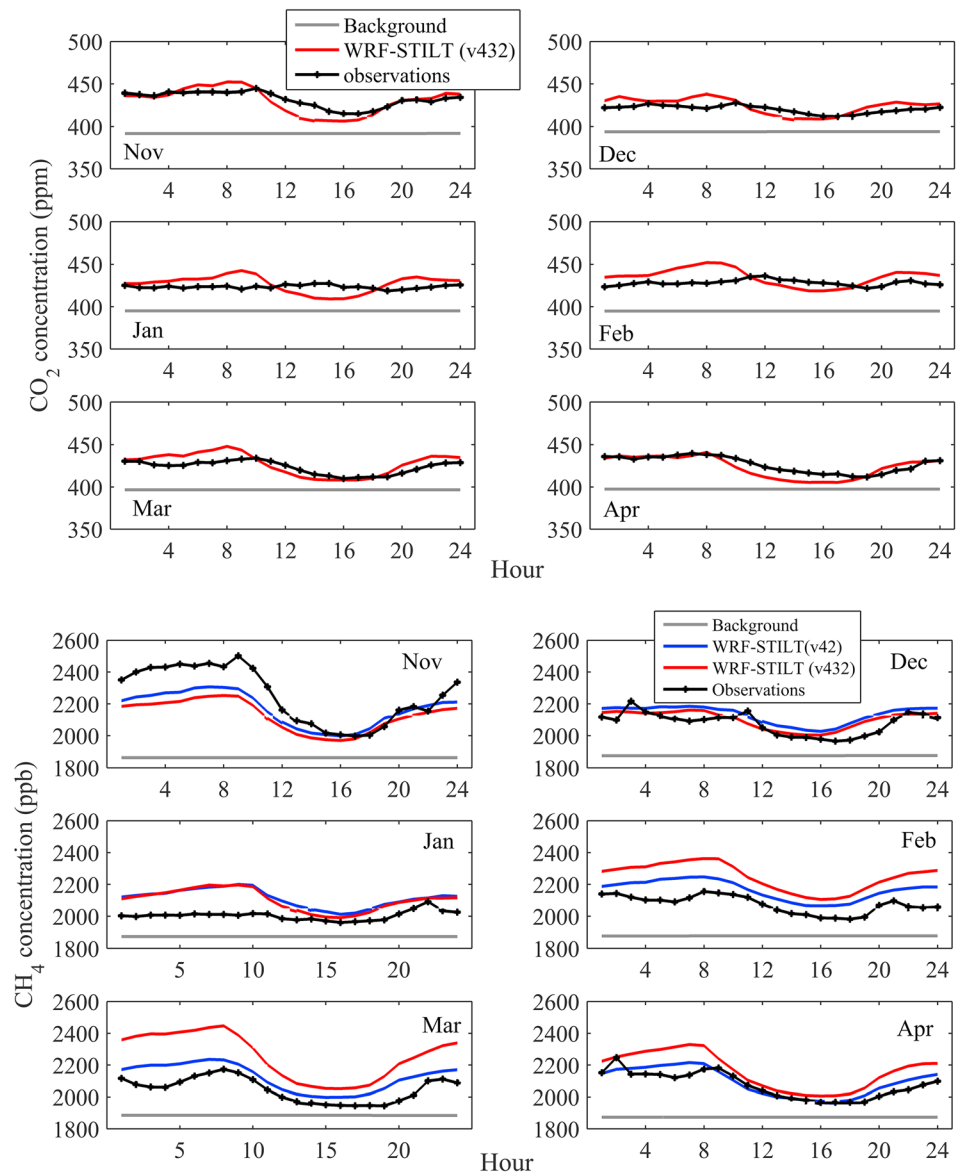
Figure 6. Monthly averaged diel variations of CO_2 and CH_4 mixing ratios from November 2010 to April 2011.

ratios in November was related to observed hot moments during some individual periods, which did not co-occur with emitted CO_2. Further, the overestimation in the other months was caused by an overestimation of CH_4 emissions from other source categories. Detailed results and examination of these source categories will be evaluated in section 3.4.3 using the SFBI approach. The results above also indicate less bias in the CO_2 inventories than for CH_4.

3.4. Constraining Anthropogenic CH_4 and CO_2 Emissions
3.4.1. Multiplicative SFs

As shown in Figure 7a the simulated CO_2 enhancements exhibited similar variations with observations for each month. Figure 7a also highlights that there is little bias in the a priori CO_2 inventories, with an overall relative model bias of 5% for these 6 months. This further supports that the uncertainty estimates of the CO_2 inventory was within 7% for the YRD for the years 2013 to 2015 (C. Hu, Liu, et al., 2018). The observed CO_2 enhancements between 2013 and 2015 were larger than for 2010–2011 for the 6-month study period. This large increase was attributed to the increased anthropogenic CO_2 emissions during these years as a result
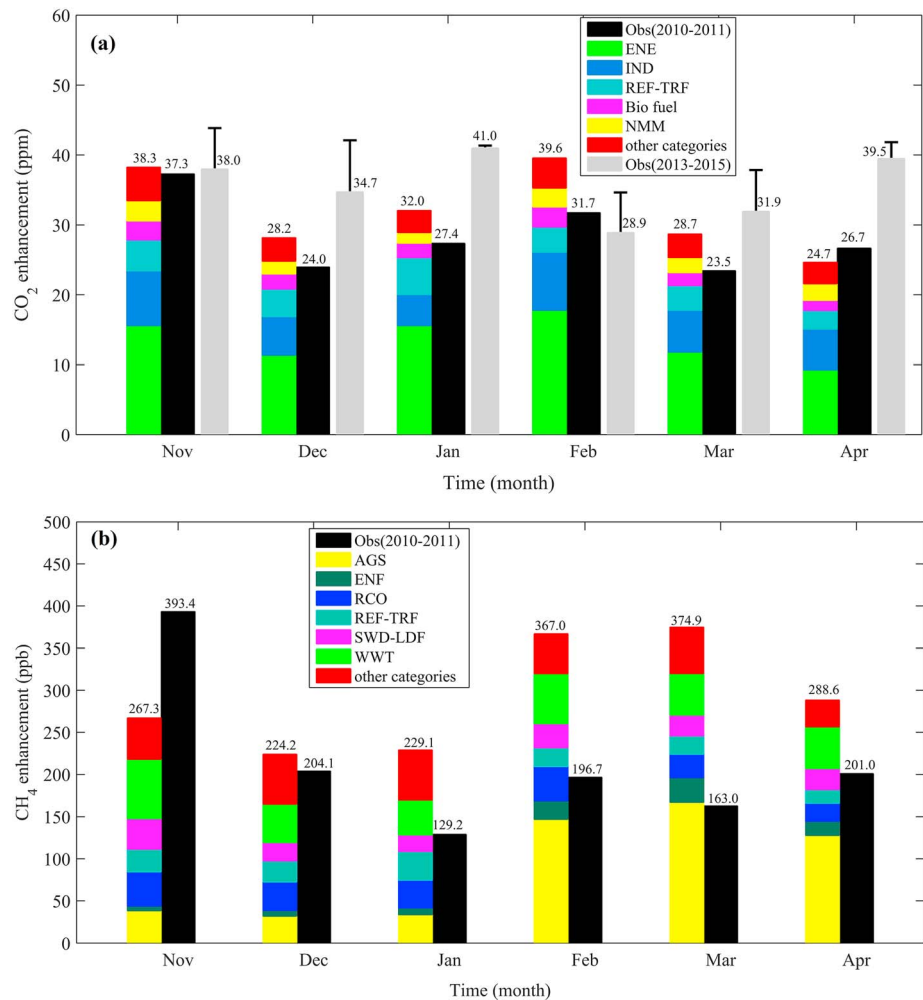
Figure 7. Comparison between modeled and observed (a) CO_2 and (b) CH_4 enhancement (Emission Database for Global Atmospheric Research v432). The major source categories are shown. Error bars indicate the standard bias of CO_2 enhancement within 3 years (2013 to 2015); subcategories are displayed for CH_4 with AGS (agricultural soil), PRO (fuel exploitation), RCO (energy for buildings), REF-TRF (oil refineries and transformation industry), WWT (waste water handling), and others (the sum of remaining categories), and with ENE (power industry), IND (combustion for manufacturing), REF-TRF (oil refineries and transformation industry), and NMM (nonmetallic minerals production) for CO_2 subcategories. ENF = enteric fermentation; SWD-LDF = solid waste landfilling.

of increased economic growth in China. Here, the GDP increased by 56% over the period 2009 to 2012. The simulated CH_4 enhancements were relatively large compared to the observations (Figure 7b). Other than November, the model results were greater than the observed CH_4 enhancements from December 2010 to April 2011, with an overall model bias of 22% (36% if November was included). Given that the WRF-STILT footprint and atmospheric transport are the same for CH_4 and CO_2, the difference in CH_4 enhancement between the model and observations resulted from the difference between the a priori inventories and the observed emissions.

The monthly MSFs for EDGAR v432 were 1.51 ($\pm$0.27), 0.92 ($\pm$0.23), 0.58 ($\pm$0.21), 0.54 ($\pm$0.14), 0.45 ($\pm$0.13), and 0.71 ($\pm$0.18) for November to April, respectively (Table 4), these uncertainties were derived from the SF uncertainties as described in section 2.4.1. These MSFs indicated that the a priori CH_4 from EDGAR v432 generally overestimated CH_4 emissions except for November, as discussed in section 3.4.3. After applying the MSFs to the monthly CH_4 emissions, the posteriori CH_4 emission estimate was 37.31 ($\pm$9.46) nmol·m^{-2}·s^{-1} and 28.3% lower than EDGAR v432. Further, we performed the same analysis for EDGAR v42 to provide a robust comparison. Here the posteriori CH_4 emission was 35.33 ($\pm$8.87) nmol·m^{-2}·s^{-1}, which

Table 4
Multiplicative Scaling Factor Analysis for CH$_4$ Emissions in the Yangtze River Delta Region

CH$_4$ inventories	Emissions	November	December	January	February	March	April	Average
EDGAR v432 (nmol·m^{-2}·s^{-1})	prior	37.31	37.06	37.25	60.63	76.63	63.50	52.06
	SFs	1.51 (±0.27)	0.92 (±0.23)	0.58 (±0.21)	0.54 (±0.14)	0.45 (±0.13)	0.71 (±0.18)	
	post	56.38(±10.03)	33.98 (±8.62)	21.57(±7.78)	32.91(±8.58)	34.19(±10.26)	44.78(±11.47)	37.31(±9.46)
EDGAR v42 (nmol·m^{-2}·s^{-1})	prior	42.44	42.44	42.44	42.44	42.44	42.44	42.44
	SFs	1.30(±0.23)	0.81 (±0.20)	0.55 (±0.20)	0.70 (±0.18)	0.70 (±0.21)	0.93 (±0.24)	
	post	55.38(±9.80)	34.24(±8.60)	23.49(±8.36)	29.74(±7.67)	29.67(±8.80)	39.45(±10.00)	35.33(±8.87)

Note. EDGAR = Emission Database for Global Atmospheric Research.

was about 16.8% lower than the a priori emission estimate from EDGAR v42. Therefore, both approaches yielded similar posteriori emissions. Taken together, these analyses support that both inventories consistently overestimated the observed CH$_4$ emissions for the YRD region. The average posteriori CH$_4$ emission was 36.32 (±9.17) nmol·m^{-2}·s^{-1} for these two approaches and 69.8 (±17.6)% of EDGAR v432 emissions.

Applying the same method to constrain CO$_2$ emissions in EDGAR v432, we obtained SFs of 1.07 (±0.20), 0.88 (±0.21), 0.91 (±0.20), 0.84 (±0.17), 0.87 (±0.22), and 1.16 (±0.26) for November 2010 to April 2011, respectively. The posteriori emissions were 4.15 (±0.92) μmol·m^{-2}·s^{-1}, approximately 5% lower than the EDGAR v432 a priori inventory of 4.38 μmol·m^{-2}·s^{-1}. These posteriori CO$_2$ emissions will be used to constrain anthropogenic CH$_4$ emissions using the FR approach below.

3.4.2. FR Results

Because the atmosphere is usually turbulently well-mixed during midday (10:00 to 17:00 local time), the mixing ratio relationship can be used to represent the flux relationship at a much larger spatial scale than during the night (Shen et al., 2014; C. Hu et al., 2018; Sargent et al., 2018). Here we used daily midday CO$_2$ and CH$_4$ average values to compute the FR from linear regression analyses from November 2010 to April 2011. The simulated FR between CH$_4$ and CO$_2$ was 0.0085 ± 0.0008 for EDGAR v432 and was significantly larger than our observations, 0.0061 ± 0.0008 (Figure 8). Since the CO$_2$ emissions are well constrained, these FR results indicate that the IPCC based CH$_4$ inventories overestimated CH$_4$ emissions for the YRD region.
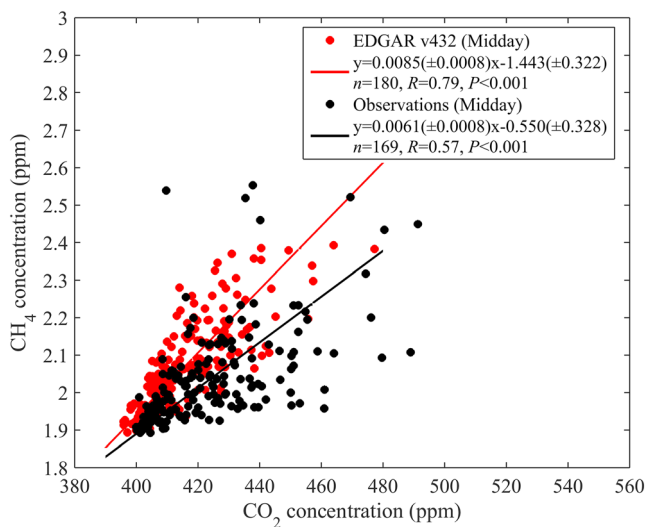

Figure 8. Scatter plots of CH$_4$ and CO$_2$ mixing ratio for both observations and simulations using prior inventories. The number of observations (*n*), regression coefficient (*R*), 95% confidence bound, and *P* values are also shown. EDGAR = Emission Database for Global Atmospheric Research.

We concluded that the FR slope difference between observations and model simulations was mainly caused by an overestimation of the anthropogenic CH$_4$ emissions, because as was shown in section 3.4.1, the a priori CO$_2$ emissions was only overestimated by 5%. Therefore, the slope difference between the model and observations implies an overestimation of the a priori CH$_4$ emissions. This FR slope difference can be applied to calibrate the a priori CH$_4$ emissions. The simulated CH$_4$ and CO$_2$ slope was 0.0085 when using EDGAR V432. As noted above in section 3.4.2 the FR can vary as a function of footprint size within the YRD as a result of the heterogeneity of CO$_2$ and CH$_4$ sources. The SF for CH$_4$ should have less uncertainty as the spatial scale increases and the heterogeneous sources become well mixed in the atmospheric boundary layer.

The FR slope differences between observations and EDGAR v432 reflected the fact that CH$_4$ emissions in EDGAR v432 were overestimated by a factor of 1.39 ± 0.12 (0.0085/0.0061), assuming the CO$_2$ emissions from EDGAR v432 represent the true values. As shown in section 3.3, the MSF approach revealed that CO$_2$ emissions were overestimated by 5%. Therefore, the corrected SF for CH$_4$ should be 1.46 ± 0.13 (1.39/0.95). The a priori anthropogenic (EDGAR v432) CH$_4$ emissions in the YRD region was 52.06 nmol·m^{-2}·s^{-1}. When applying the SF of 1.46 ± 0.13, the calibrated CH$_4$ emission was 35.66 (±2.92) nmol·m^{-2}·s^{-1}.

Table 5
Scaling Factors (dpost) and Posteriori CH₄ Emissions (nmol·m^{-2}·s^{-1}) Derived From the SFBI Approach

Categories	Strategy	Emissions	November	December	January	February	March	April	Average
AGS		priori	8.26	8.00	8.00	25.57	41.75	31.21	20.46
	1	dpost	1.08	1.01	0.71	0.56	0.45	0.42	0.70
		post	8.92	8.04	5.70	14.27	18.68	13.14	11.46
	2	dpost	1.24	1.03	0.68	0.43	0.29	0.40	0.68
		post	10.22	8.23	5.41	10.94	12.22	12.37	9.90
PRO		priori	8.99	8.70	8.70	9.63	8.70	8.99	8.95
	1	dpost	0.70	0.31	0.47	0.89	0.89	0.88	0.69
		post	6.33	2.70	4.06	8.58	7.73	7.89	6.22
	2	dpost	0.94	0.36	0.43	0.86	0.83	0.87	0.72
		post	8.45	3.16	3.74	8.24	7.25	7.86	6.45
RCO		priori	5.53	6.31	6.50	6.35	4.97	3.95	5.60
	1	dpost	0.97	0.94	0.69	0.90	0.93	0.95	0.90
		post	5.39	5.93	4.49	5.69	4.60	3.73	4.97
	2	dpost	1.13	0.97	0.66	0.86	0.90	0.94	0.91
		post	6.22	6.12	4.28	5.45	4.46	3.71	5.04
REF		priori	0.93	0.90	0.90	1.00	0.90	0.93	0.92
	1	dpost	0.68	0.66	0.59	0.93	0.90	0.77	0.75
		post	0.63	0.59	0.53	0.92	0.81	0.71	0.70
	2	dpost	0.88	0.69	0.57	0.91	0.88	0.77	0.78
		post	0.81	0.62	0.51	0.90	0.79	0.72	0.73
WWT		priori	7.67	7.42	7.42	8.21	7.42	7.67	7.63
	1	dpost	0.92	0.87	0.55	0.85	0.87	0.87	0.82
		post	7.08	6.42	4.08	6.97	6.45	6.68	6.28
	2	dpost	1.17	0.91	0.51	0.80	0.82	0.86	0.84
		post	8.98	6.72	3.81	6.53	6.08	6.58	6.45
Others		priori	5.91	5.72	5.73	9.89	12.89	10.78	8.49
	1	dpost	0.93	0.87	0.66	0.83	0.81	0.84	0.82
		post	5.50	4.95	3.77	8.17	10.48	9.02	6.98
	2	dpost	1.12	0.90	0.63	0.77	0.74	0.82	0.83
		post	6.64	5.15	3.58	7.58	9.53	8.86	6.89
All categories		priori	37.29	37.04	37.24	60.65	76.63	63.52	52.06
	1	post	33.84	28.63	22.64	44.60	48.75	41.18	36.61
	2	post	41.32	30.00	21.33	39.64	40.33	40.09	35.45

Note. Results of both strategies (strategy 1 and 2) are shown. SFBI = scale factor Bayesian inversion; AGS = agricultural soil; PRO = fuel exploitation; RCO = energy for buildings; REF = oil refineries and transformation industry; WWT = waste water handling; Others = the sum of remaining categories.

Based on these analyses, we also retrieved the background CH₄ mixing ratio following the method of Wang et al. (2010). For example, assuming a background CO₂ value of 395 ppm in winter we estimated a background CH₄ value of $(395 \times 0.0061 - 0.55) \times 1{,}000 = 1{,}859.5$ ppb, where the slope of 0.061 and intercept of -0.55 was derived from the observations shown in Figure 8. The average CH₄ background mixing ratio based on the two NOAA sites (WLG and UUM) was 1,874.6 ppb and in reasonably good agreement. These results suggest that the WLG (36°17′N, 100°54′E, 3,810-m height) and UUM (44°27′N, 111°01′E, 1,007-m height) sites can provide a reasonable estimate of the background CH₄ mixing ratio.

3.4.3. SFBI

Results from the SFBI analyses are summarized in Table 5. Both strategies of handling the background CH₄ mixing ratio within the inversion (see details in section 2.4.3 for these two strategies) generated similar results for the different source categories. Further, the sum of all CH₄ categories yielded posteriori emissions of 36.61 ($\pm$14.69) for strategy 1 and 35.45 ($\pm$13.81) nmol·m^{-2}·s^{-1} for strategy 2. The uncertainties presented here were calculated using the Monte Carlo approach. The results for both strategies were 70.3 ($\pm$28.2)% and 68.1 ($\pm$26.5)% of the a priori EDGAR v432 inventory emissions.

The SFs derived from the SFBI analyses indicate that CH₄ emissions from PRO were generally overestimated. The SF varied between 0.31 and 0.94 during 6 months for both strategies. The average posteriori

emissions were 6.22 nmol·m^{-2}·s^{-1} for strategy 1 and 6.45 nmol·m^{-2}·s^{-1} for strategy 2, indicating an overestimate of 30.8% (strategy 1) and 28.0% (strategy 2) when compared with the EDGAR v432 inventory emissions. Further, the SFBI analyses also support that emissions from AGS were also overestimated from January to April. Note that monthly EDGAR v432 inventory has already considered the seasonal variation of AGS (Figure S1), and it reflects the mismatch between the monthly inventory and true emissions. As noted, rice cultivation is the only contributor to AGS emission (Janssens-Maenhout et al., 2017). Here, the SFBI inversion results for AGS contain all CH$_4$ emissions from agricultural lands, and include intensive irrigation systems such as canals and ditches in the YRD area (i.e., retained water in the winter). Methane emissions from these irrigation systems are also included in our posteriori estimate for AGS. The posteriori emissions were 11.44 and 9.88 nmol·m^{-2}·s^{-1} and approximately 44.0% and 51.7% lower than the a priori emissions EDGAR v432. The underestimation in November was mainly attributed to energy for building and WWT. The SFs for the other source categories did not reveal large biases when compared with the inventory emission data. Based on the SFBI analyses, it appears that the EDGAR v432 inventory emissions are overestimated for the YRD region, which is caused primarily by an overestimation of emissions from PRO and rice cultivation categories. In general, rice cultivation is the largest CH$_4$ source in the YRD region and accounts for 29.6% of the total anthropogenic emissions during our study period (November 2010 to April 2011). WWT was the second largest source accounting for 17.7% and PRO ranked third and accounted for 17.6%.

To evaluate the posteriori CH$_4$ emissions, we applied the SFBI SFs to the corresponding CH$_4$ emission source categories and simulated CH$_4$ mixing ratios again (red color in Figure 9). As shown, the large discrepancy between observations and model simulations decreased significantly following the SFBI optimization. The posteriori simulated CH$_4$ mixing ratios and enhancements show very good agreement with the observations (Figure 9a). Analysis of the weekly average values (Figure 9b) show that the slope decreased from 1.22 to 0.95 for the posteriori emissions versus the a priori emissions and that the R^2 between the observed weekly averaged CH$_4$ enhancements with the simulated results improved from 0.003 to 0.42.

3.4.4. Comparison of Three Top-Down Methods

Based on three different "top-down" methods, we have constrained anthropogenic CH$_4$ emissions for the YRD area, one of the world's most densely populated regions. We have estimated CH$_4$ emissions to be 36.32 ($\pm$9.17), 35.66 ($\pm$2.92), and 36.03($\pm$14.25) nmol·m^{-2}·s^{-1} using the MSF, FR, and SFBI approaches, respectively (Figure 10). Overall, these posteriori emissions were 30.2($\pm$17.6)%, 31.5 ($\pm$5.6)%, and 30.8 ($\pm$27.4)% lower than the a priori EDGAR v432 inventory (52.06 nmol·m^{-2}·s^{-1}). The Bayesian inversion approach also indicates that the large bias is mainly attributed by an overestimation of emissions from fossil fuel exploitation and rice cultivation. When averaging all three approaches the anthropogenic CH$_4$ emissions in the YRD area was estimated to be 36.00 ($\pm$8.78) nmol·m^{-2}·s^{-1}. Therefore, EDGAR v432 overestimated the anthropogenic CH$_4$ emissions by 44.6% on average.

When excluding AGS emissions, the sum of remaining anthropogenic CH$_4$ emission was 4.59 ($\pm$1.12) Tg in 2010 for the YRD area. We further calculated the anthropogenic CH$_4$ emissions in the cold/dormant period and compared it with the annual average in 2010 (EDGAR v432). The total anthropogenic CH$_4$ emissions were 52.06 nmol·m^{-2}·s^{-1} for the cold/dormant period and 47.39 nmol·m^{-2}·s^{-1} for the annual average. AGS emissions were 20.46 and 18.17 nmol·m^{-2}·s^{-1}, for these periods, respectively. In 2010–2011, the a priori anthropogenic CH$_4$ emissions were 9.46 Tg for YRD and the posteriori total anthropogenic CH$_4$ emissions were 6.52($\pm$1.59) Tg for the YRD area.

4. Discussion

Based on the bottom-up IPCC methodology, Shen et al. (2014) concluded that anthropogenic CH$_4$ emissions were 5.07 ($\pm$0.76) Tg for the YRD in 2009. Their estimate is in reasonably good agreement with our top-down estimates. Our findings also agree well with Thompson et al. (2015) who constrained CH$_4$ emissions for East Asia by using flask and in situ measurements in combination with an atmospheric transport model and Bayesian inversion method. They concluded that EDGAR v42 overestimated emissions in China by 29% between 2000 and 2011. Xiao et al. (2004) conducted aircraft observations of the Asian outflow in 2000. By applying the FR method they concluded that the Streets et al. (2003) inventory was biased low by about 40%. They attributed this underestimation to a low bias in livestock and landfill sources in China. From both
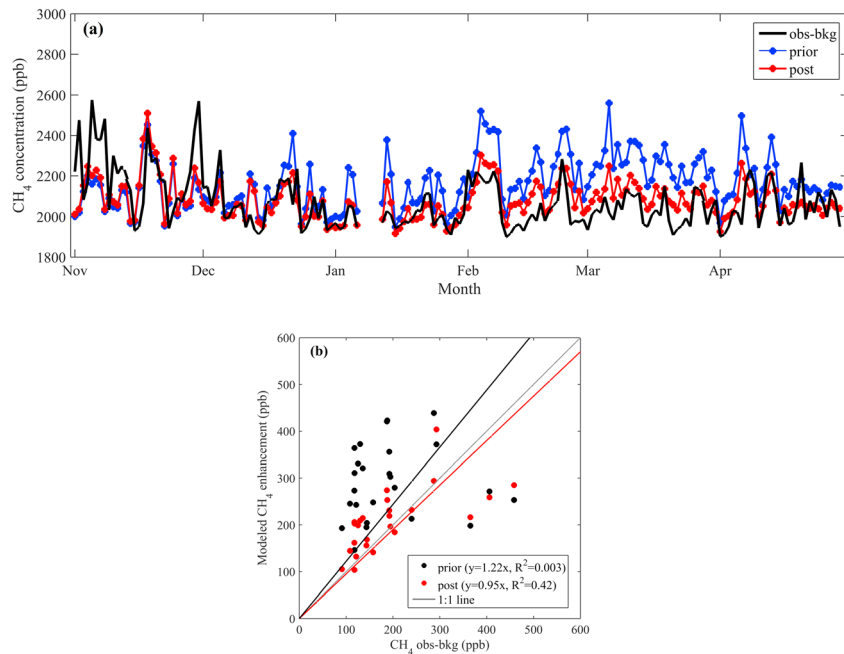
Figure 9. Comparison between observed CH_4 enhancements with modeled enhancement by using prior and post inventory CH_4 emissions for (a) daily CH_4 concentrations and (b) weekly averaged CH_4 enhancements.

observations and model simulations in Asia, Tohjima et al. (2014) derived 10 years of ΔCH_4: ΔCO_2 enhancement correlations in winter (November to March) and compared anthropogenic CH_4 emissions (without rice cultivation) with the EDGAR v42 inventory. They found reasonably good agreement between their results and EDGAR v42 from 1998 to 2002, while EDGAR v42 showed significantly higher CH_4 emissions and an increasing trend in emissions between 2002 and 2010. This was attributed to an overestimating of coal mining emissions.

The agricultural sector accounts for about 50% of global GHG emissions (Wang et al., 2012). Agricultural CH_4 emissions include emissions from crop cultivation (rice and wheat), fertilizer use, and animal waste. In China, rice cultivation accounted for nearly 21.5% (or 14.2 Tg) of total anthropogenic CH_4 emissions in 2012 (Janssens-Maenhout et al., 2017). The uncertainties in these CH_4 emissions relate to cropping area,
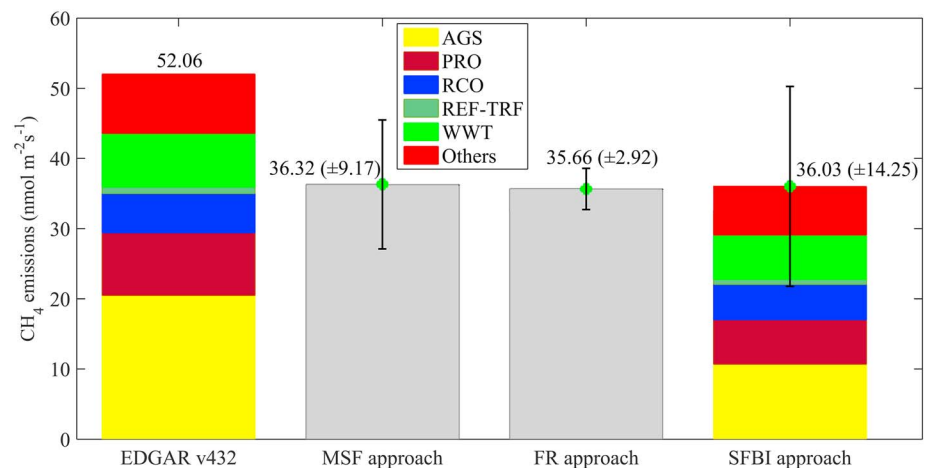

Figure 10. Comparison of posteriori anthropogenic CH_4 emissions constrained by three top-down methods with the a priori EDGAR v432 inventory; subcategories are displayed with AGS (agricultural soil), PRO (fuel exploitation), RCO (energy for buildings), REF-TRF (oil refineries and transformation industry), WWT (waste water handling), and Others (the sum of remaining categories).

crop properties, field irrigation information, manure production, and applied organic matter amendments (Khalil & Butenhoff, 2008). Excluding cropping area, all of these factors can influence the CH_4 EFs. The EF for rice cultivation in China is 5 times larger than India in inventories used to calculate global CH_4 emissions for EDGAR v432 (Janssens-Maenhout et al., 2017). This difference has been attributed to the multiple harvests per year from irrigated rice fields (China) than rain-fed (India). The EFs for irrigated rice fields in China have decreased by about one third for the new farming practices established over the period 1970 to 2000 (Li et al., 2002). Our knowledge of these changes in land management practices is generally poor, not well represented in inventories, and highly uncertain at fine spatial and temporal scales (i.e., monthly and regional scale). This can lead to large biases in model upscaling. A recent study by Liu et al. (2016) indicated that land use changes in the YRD area can alter CH_4 emissions by up to 48% depending on the land use area associated with rice paddies versus aquaculture. Therefore, lack of up-to-date land use information can lead to large biases in CH_4 emissions at the regional scale. Based on process-based models and applying uncertainty analyses, Zhang et al. (2014) found that the CH_4 emissions from rice cultivation varied between 4.5 and 8.7 Tg/year in China (95% confidence interval) with a propagated uncertainty of 100% at the country scale. Estimates based on the IPCC methodology indicate that global CH_4 emissions from rice cultivation ranges between 14.8 and 41.5 Tg/year, yielding an uncertainty on the order of 300% (Yan et al., 2009).

Many studies have also shown large variations in wintertime CH_4 emissions and EFs based on field experiments. For example, a 4-year field measurement campaign of CH_4 emissions from rice cultivation in Jiangxi, China, demonstrated that wintertime (November to April) average emissions varied between 0.02 and 0.18 mg·m^{-2}·hr^{-1} (Zhang et al., 2016). Our posteriori CH_4 emission estimate for rice cultivation was 0.57 to 0.66 mg·m^{-2}·hr^{-1}. Tian et al. (2015) (in Chinese) conducted straw incorporation experiments for rice in winter and found that the CH_4 emissions peaked at 10 mg·m^{-2}·hr^{-1}. Experiments conducted in the U.S. Corn Belt peaked at 0.55 mg·m^{-2}·hr^{-1} for tilled soils and 0.21 mg·m^{-2}·hr^{-1} for no-till soils (Ussiri et al., 2009). These emission differences illustrate the large local scale uncertainty related to agricultural management practices. Here, we see that field scale agricultural studies indicate that the differences in emissions among similar agricultural lands can be on the order of 300%.

The uncertainty associated with urban/industrial CH_4 emissions is also reported to be relatively large. Peng et al. (2016) applied localized EFs to calculate CH_4 emissions in China and concluded that CH_4 emissions were 18% to 36% lower than the results obtained by using the IPCC default EF method. Also, for low quality coal, EFs for underground coal mines in China should be lower than that recommended for Europe (Liu et al., 2015; Peng et al., 2016). Based on on-road measurements, N. Hu et al. (2018) found that CH_4 emissions from natural gas vehicles were underestimated by 800% in China. This was attributed to IPCC EFs that were too low. A recent study by Miller et al. (2019) also found that CH_4 coal mining emissions based on EDGAR v432 were large compared to inverse modeling results for China. Large biases were also reported for coal mining CO_2 EFs that were obtained through field experiments in different provinces throughout China. Here, the EFs varied between 0.74 and 36 m^3/t (Zhu et al., 2017). These results indicated that EFs related to urban/industrial processes can have large uncertainties in different regions and EFs for some regions and some categories can vary considerably when compared with default EFs recommended by IPCC method.

Quantifying the spatial and temporal relationships between GHG mixing ratios (emissions) and urban growth (i.e., land use change, population and economic growth) is essential in developing mitigation GHG strategies, where long-term GHG observations are needed. A recent study examined 10 years of GHG mixing ratios in Salt Lake City, USA, observed a nonlinear relationship between population and emissions. They concluded that there was an increase of emissions with the increase in development of urban areas. They also found that emissions were relatively stable when urban development was steady (Mitchell et al., 2018). Here, the YRD is undergoing rapid economic development and population and urban growth. Therefore, considerably larger GHG emissions are projected in the near future. Comparing CO_2 emissions in 2009 and 2012 for YRD indicates that CO_2 emissions increased by a staggering 70%. This corresponded with a 56% increase in GDP (Shen et al., 2014; Xu et al., 2017). Clearly, there is an important need to establish long-term GHG observation networks within rapidly developing urban regions to improve our understanding of emissions and to assess if mitigation strategies are effective.

5. Conclusions

Here, we combined atmospheric observations and three inverse modeling approaches to help constrain and reduce the uncertainty in anthropogenic CH_4 emissions for YRD. Our data and analyses support the following conclusions:

1. The a posteriori anthropogenic CH_4 emissions in YRD area are estimated to be 36.3 ($\pm$9.2), 35.7 ($\pm$2.9), and 36.0($\pm$14.3) nmol·m^{-2}·s^{-1}, for the MSF, FR, and SFBI approaches, respectively. These estimates show high consistency and were 30.8 ($\pm$16.9)% lower than EDGAR v432 inventories (52.1 nmol·m^{-2}·s^{-1}). The annual anthropogenic CH_4 emission is estimated at 6.52 ($\pm$1.59) Tg for the YRD area using these top-down methods.

2. The overestimation of the anthropogenic CH_4 emissions by EDGAR v432 was mainly related to a high bias in fossil fuel exploitation and AGS (rice cultivation). Fossil fuel exploitation and AGS emissions were overestimated by 41.3% and 91.6%, respectively. AGS was the largest regional source and accounted for 29.6% of the regional CH_4 budget.

3. Our analyses indicate that fossil fuel exploitation and AGS emissions in the a priori inventory EDGAR v432 are poorly estimated with relatively large uncertainties in EFs at the regional and monthly scale. These findings imply greater need for bottom-up field experiments at the appropriate spatial scale (i.e., field scale) that can be used to help constrain CH_4 emissions in these target areas.

References

Cai, B., Lou, Z., Wang, J., Geng, Y., Sarkis, J., Liu, J., & Gao, Q. (2018). CH4 mitigation potentials from China landfills and related environmental co-benefits. *Science Advances*, *4*(7), eaar8400. https://doi.org/10.1126/sciadv.aar8400

Cao, C., Lee, X., Liu, S., Schultz, N., Xiao, W., Zhang, M., & Zhao, L. (2016). Urban heat islands in China enhanced by haze pollution. *Nature Communications*, *7*(1). https://doi.org/10.1038/ncomms12509

Chen, Z., Griffis, T. J., Baker, J. M., Millet, D. B., Wood, J. D., Dlugokencky, E. J., et al. (2018). Source partitioning of methane emissions and its seasonality in the U.S. Midwest. *Journal of Geophysical Research: Biogeosciences*, *123*, 646–659. https://doi.org/10.1002/2017JG004356

Chen, Z., Griffis, T. J., Millet, D. B., Wood, J. D., Lee, X., Baker, J. M., et al. (2016). Partitioning N_2O emissions within the U.S. Corn Belt using an inverse modeling approach. *Global Biogeochemical Cycles*, *30*, 1192–1205. https://doi.org/10.1002/2015GB005313

Dlugokencky, E. J., Bruhwiler, L., White, J. W. C., Emmons, L. K., Novelli, P. C., Montzka, S. A., et al. (2009). Observational constraints on recent increases in the atmospheric CH4 burden. *Geophysical Research Letters*, *36*, L18803. https://doi.org/10.1029/2009GL039780

Duren, R. M., & Miller, C. E. (2012). Measuring the carbon emissions of megacities. *Nature Climate Change*, *2*(8), 560–562. https://doi.org/10.1038/nclimate1629

Fang, S. X., Zhou, L. X., Masarie, K. A., Xu, L., & Rella, C. W. (2013). Study of atmospheric CH_4 mole fractions at three WMO/GAW stations in China. *Journal of Geophysical Research: Atmospheres*, *118*, 4874–4886. https://doi.org/10.1002/jgrd.50284

Food and Agricultural Organization (FAO). The state of world fisheries and aquaculture; Food and Agricultural Organization of the United Nations: Rome, Italy, 2014.

Gerbig, C., Lin, J. C., Wofsy, S. C., Daube, B. C., Andrews, A. E., Stephens, B. B., et al. (2003). Toward constraining regional-scale fluxes of CO_2 with atmospheric observations over a continent: 2. Analysis of COBRA data using a receptor-oriented framework. *Journal of Geophysical Research*, *108*(D24), 4757. https://doi.org/10.1029/2003JD003770

Graven, H., Fischer, M. L., Lueker, T., Jeong, S., Guilderson, T. P., Keeling, R. F., et al. (2018). Assessing fossil fuel CO2 emissions in California using atmospheric observations and models. *Environmental Research Letters*, *13*(6). https://doi.org/10.1088/1748-9326/aabd43

Griffis, T. J., Chen, Z., Baker, J. M., Wood, J. D., Millet, D. B., Lee, X., et al. (2017). Nitrous oxide emissions are enhanced in a warmer and wetter world. *Proceedings of the National Academy of Sciences*, *114*(45), 12081–12085. https://doi.org/10.1073/pnas.1704552114

Guo, J., Miao, Y., Zhang, Y., Liu, H., Li, Z., Zhang, W., et al. (2016). The climatology of planetary boundary layer height in China derived from radiosonde and reanalysis data. *Atmospheric Chemistry and Physics*, *16*(20), 13309–13319. https://doi.org/10.5194/acp-16-13309-2016

Gurney, K. R., Liang, J., Patarasuk, R., O'Keeffe, D., Huang, J., Hutchins, M., et al. (2017). Reconciling the differences between a bottom-up and inverse-estimated FFCO2 emissions estimate in a large US urban area. *Elementa Science of the Anthropocene*, *5*(0), 44. https://doi.org/10.1525/elementa.137

Gurney, K. R., Mendoza, D. L., Zhou, Y., Fischer, M. L., Miller, C. C., Geethakumar, S., & de la Rue du Can, S. (2009). High Resolution Fossil Fuel Combustion CO2 Emission Fluxes for the United States. *Environmental Science & Technology*, *43*(14), 5535–5541. https://doi.org/10.1021/es900806c

Hedelius, J. K., Liu, J., Oda, T., Maksyutov, S., Roehl, C. M., Iraci, L. T., et al. (2018). Southern California megacity CO_2, CH_4, and CO flux estimates using ground- and space-based remote sensing and a Lagrangian model. *Atmospheric Chemistry and Physics*, *18*(22), 16271–16291. https://doi.org/10.5194/acp-18-16271-2018

Hopkins, F. M., Kort, E. A., Bush, S. E., Ehleringer, J. R., Lai, C.-T., Blake, D. R., & Randerson, J. T. (2016). Spatial patterns and source attribution of urban methane in the Los Angeles Basin. *Journal of Geophysical Research: Atmosphere*, *121*, 2490–2507. https://doi.org/10.1002/2015JD024429

Hu, C., Griffis, T. J., Lee, X., Millet, D. B., Chen, Z., Baker, J. M., & Xiao, K. (2018). Top-down constraints on anthropogenic CO_2 emissions within an agricultural-urban landscape. *Journal of Geophysical Research: Atmospheres*, *123*, 4674–4694. https://doi.org/10.1029/2017JD027881

Hu, C., Liu, S., Wang, Y., Zhang, M., Xiao, W., Wang, W., & Xu, J. (2018). Anthropogenic CO_2 emissions from a megacity in the Yangtze River Delta of China. *Enviromental Science and Pollution Research*, *25*(23), 23157–23169. https://doi.org/10.1007/s11356-018-2325-3

Hu, N., Liu, S., Gao, Y., Xu, J., Zhang, X., Zhang, Z., & Lee, X. (2018). Large methane emissions from natural gas vehicles in Chinese cities. *Atmospheric Environment*, *187*, 374–380. https://doi.org/10.1016/j.atmosenv.2018.06.007

International Energy Agency: IEA World Energy Outlook2008, Chap.8, 179-193,2008. Intergovernmental Panel on Climate Change (IPCC) Climate change 2013: The physical science basis, contribution of Working Group I to the Fifth Assessment Report of the Intergovernmental Panel on Climate Change; Cambridge University Press: Cambridge, 2013.

Janssens-Maenhout, G., Crippa, M., Guizzardi, D., Muntean, M., Schaaf, E., Dentener, F., et al. (2017). EDGAR v4.3.2 global atlas of the three major greenhouse gas emissions for the period 1970–2012. *Earth System Science Data Discussions*, 1–55. https://doi.org/10.5194/essd-2017-79

Jiang, F., Wang, H. M., Chen, J. M., Machida, T., Zhou, L. X., Ju, W. M., et al. (2014). Carbon balance of China constrained by CONTRAIL aircraft CO_2 measurements. *Atmospheric Chemistry and Physics*, *14*(18), 10133–10144. https://doi.org/10.5194/acp-14-10133-2014

Khalil, M. A. K., & Butenhoff, C. L. (2008). Spatial variability of methane emissions from rice fields and implications for experimental design. *Journal of Geophysical Research*, *113*, G00A09. https://doi.org/10.1029/2007JG000517

Kim, S. Y., Millet, D. B., Hu, L., Mohr, M. J., Griffis, T. J., Wen, D., et al. (2013). Constraints on carbon monoxide emissions based on tall tower measurements in the U.S. upper midwest. *Environmental Science and Technology*, *47*(15). https://doi.org/10.1021/es4009486

Kirschke, S., Bousquet, P., Ciais, P., Saunois, M., Canadell, J. G., Dlugokencky, E. J., et al. (2013). Three decades of global methane sources and sinks. *Nature Geoscience*, *6*(10), 813–823. https://doi.org/10.1038/ngeo1955

Kort, E. A., Frankenberg, C., Costigan, K. R., Lindenmaier, R., Dubey, M. K., & Wunch, D. (2014). Four corners: The largest US methane anomaly viewed from space. *Geophysical Research Letters*, *41*, 6898–6903. https://doi.org/10.1002/2014GL061503

Lee, X., Liu, S., Xiao, W., Wang, W., Gao, Z., Cao, C., et al. (2014). The Taihu eddy flux network: An observational program on energy, water, and greenhouse gas fluxes of a large freshwater lake. *Bulletin of the American Meteorological Society*, *95*(10), 1583–1594. https://doi.org/10.1175/BAMS-D-13-00136.1

Li, C., Qiu, J., Frolking, S., Xiao, X., Salas, W., Moore, B.III, et al. (2002). Reduced methane emissions from large-scale changes in water management of China's rice paddies during 1980–2000. *Geophysical Research Letters*, *29*(20), 1972. https://doi.org/10.1029/2002GL015370

Lin, J. C. (2003). A near-field tool for simulating the upstream influence of atmospheric observations: The Stochastic Time-Inverted Lagrangian Transport (STILT) model. *Journal of Geophysical Research*, *108*(D16), 4493. https://doi.org/10.1029/2002JD003161

Liu, S., Hu, Z., Wu, S., Li, S., Li, Z., & Zou, J. (2016). Methane and nitrous oxide emissions reduced following conversion of rice paddies to inland crab-fish aquaculture in southeast China. *Environmental Science and Technology*, *50*(2), 633–642. https://doi.org/10.1021/acs.est.5b04343

Liu, Z., Guan, D., Wei, W., Davis, S. J., Ciais, P., Bai, J., et al. (2015). Reduced carbon emission estimates from fossil fuel combustion and cement production in China. *Nature*, *524*(7565), 335–338. https://doi.org/10.1038/nature14677

Miller, S. M., Michalak, A. M., Detmers, R. G., Hasekamp, O. P., Bruhwiler, L. M. P., & Schwietzke, S. (2019). China's coal mine methane regulations have not curbed growing emissions. *Nature Communications*, *10*(1), 303–308. https://doi.org/10.1038/s41467-018-07891-7

Miller, S. M., Wofsy, S. C., Michalak, A. M., Kort, E. A., Andrews, A. E., Biraud, S. C., et al. (2013). Anthropogenic emissions of methane in the United States. *Proceedings of the National Academy of Sciences*, *110*(50), 20018–20022. https://doi.org/10.1073/pnas.1314392110

Mitchell, L. E., Lin, J. C., Bowling, D. R., Pataki, D. E., Strong, C., Schauer, A. J., et al. (2018). Long-term urban carbon dioxide observations reveal spatial and temporal dynamics related to urban characteristics and growth. *Proceedings of the National Academy of Sciences*, *115*(12), 2912–2917. https://doi.org/10.1073/pnas.1702393115

National Bureau of Statistics of China (2010). *China statistical yearbook*, (p. 1032). China Statistics Press. [Available online at http://www.stats.gov.cn/tjsj/ndsj/2010/indexch.htm.]

Nehrkorn, T., Eluszkiewicz, J., Wofsy, S. C., Lin, J. C., Gerbig, C., Longo, M., & Freitas, S. (2010). Coupled Weather Research and Forecasting-StochasticTime-Inverted Lagrangian Transport (WRF-STILT) model. *Meteorology and Atmospheric Physics*, *107*(1-2), 51–64. https://doi.org/10.1007/s00703-010-0068-x

Nisbet, E. G., Dlugokencky, E. J., & Bousquet, P. (2014). Methane on the rise—Again. *Science*, *343*(6170), 493–495. https://doi.org/10.1126/science.1247828

Nisbet, E. G., Dlugokencky, E. J., Manning, M. R., Lowry, D., Fisher, R. E., France, J. L., et al. (2016). Rising atmospheric methane: 2007–2014 growth and isotopic shift. *Global Biogeochemical Cycles*, *30*, 1356–1370. https://doi.org/10.1002/2016GB005406

Nisbet, E. G., Manning, M. R., Dlugokencky, E. J., Fisher, R. E., Lowry, D., Michel, S. E., et al. (2019). Very Strong Atmospheric Methane Growth in the 4 Years 2014–2017: Implications for the Paris Agreement. *Global Biogeochemical Cycles*, *33*. https://doi.org/10.1029/2018GB006009

Oda, T., & Maksyutov, S. (2016). A very high-resolution (1 km × 1 km) global fossil fuel CO_2 emission inventory derived 425 using a point source database and satellite observations of nighttime lights. *Atmospheric Chemistry and Physics*, *11*(2), 543–556. http://doi.org/10.5194/acp-11-543-2011

Peng, S., Piao, S., Bousquet, P., Ciais, P., Li, B., Lin, X., et al. (2016). Inventory of anthropogenic methane emissions in mainland China from 1980 to 2010. *Atmospheric Chemistry and Physics*, *16*(22), 14545–14562. https://doi.org/10.5194/acp-16-14545-2016

Peters, W., Jacobson, A. R., Sweeney, C., Andrews, A. E., Conway, T. J., Masarie, K., et al. (2007). An atmospheric perspective on North American carbon dioxide exchange: CarbonTracker. *Proceedings of the National Academy of Sciences*, *104*(48), 18925–18930. https://doi.org/10.1073/pnas.0708986104

Pison, I., Berchet, A., Saunois, M., Bousquet, P., Broquet, G., Conil, S., et al. (2018). How a European network may help with estimating methane emissions on the French national scale. *Atmospheric Chemistry and Physics*, *18*(5), 3779–3798. https://doi.org/10.5194/acp-18-3779-2018

Rayner, P. J., Raupach, M. R., Paget, M., Peylin, P., & Koffi, E. (2010). A new global gridded data set of CO_2 emissions from fossil fuel combustion: Methodology and evaluation. *Journal of Geophysical Research*, *115*, D19306. https://doi.org/10.1029/2009JD013439

Rosenzweig, C., Solecki, W., Hammer, S. A., & Mehrotra, S. (2010). Cities lead the way in climate-change action. *Nature*, *467*(7318), 909–911. https://doi.org/10.1038/467909a

Salmon, O. E., Shepson, P. B., Ren, X., He, H., Hall, D. L., Dickerson, R. R., et al. (2018). Top-Down Estimates of NOxand CO Emissions From Washington, D.C.-Baltimore During the WINTER Campaign. *Journal of Geophysical Research: Atmospheres*, *123*, 7705–7724. https://doi.org/10.1029/2018JD028539

Sargent, M., Barrera, Y., Nehrkorn, T., Hutyra, L. R., Gately, C. K., Jones, T., et al. (2018). Anthropogenic and biogenic CO2fluxes in the Boston urban region. *Proceedings of the National Academy of Sciences*, *115*(29), 7491–7496. https://doi.org/10.1073/pnas.1803715115

Saunois, M., Jackson, R. B., Bousquet, P., Poulter, B., & Canadell, J. G. (2016). The growing role of methane in anthropogenic climate change. *Environmental Research Letters*, *11*(12). https://doi.org/10.1088/1748-9326/11/12/120207

Shen, S., Yang, D., Xiao, W., Liu, S., & Lee, X. (2014). Constraining anthropogenic CH_4 emissions in nanjing and the Yangtze River Delta, China, using atmospheric CO_2 and CH_4 mixing ratios. *Advances in Atmospheric Sciences*, *31*(6), 1343–1352. https://doi.org/10.1007/s00376-014-3231-3

Streets, D. G., Bond, T. C., Carmichael, G. R., Fernandes, S. D., Fu, Q., He, D., et al. (2003). An inventory of gaseous and primary aerosol emissions in Asia in the year 2000. *Journal of Geophysical Research*, *108*(D21), 8809. https://doi.org/10.1029/2002JD003093

Thompson, R. L., Stohl, A., Zhou, L. X., Dlugokencky, E., Fukuyama, Y., Tohjima, Y., et al. (2015). Methane emissions in East Asia for 2000–2011 estimated using an atmospheric Bayesian inversion. *Journal of Geophysical Research: Atmospheres*, *120*, 4352–4369. https://doi.org/10.1002/2014JD022394

Thoning, K. W., Tans, P. P., & Komhyr, W. D. (1989). Atmospheric carbon dioxide at Mauna Loa observatory 2. Analysis of the NOAA/GMCC data, 1974–1985. *Journal of Geophysical Research*, *94*(D6), 8549–8565. https://doi.org/10.1029/JD094iD06p08549

Tian, K., Zhang, L., Zhong, X., et al. (2015). Effects of rice straw and winter green manure incorporations on grain yields and methane emissions of double-season rice (*Oryza sativa*) field in south China. *Journal of Agro-Enviroment Science*, *34*(3), 592–598. https://doi.org/10.11654/jaes.2015.03.024 in Chinese

Tohjima, Y., Kubo, M., Minejima, C., Mukai, H., Tanimoto, H., Ganshin, A., et al. (2014). Temporal changes in the emissions of CH_4 and CO from China estimated from CH_4/CO_2 and CO/CO_2 correlations observed at Hateruma Island. *Atmospheric Chemistry and Physics*, *14*(3), 1663–1677. https://doi.org/10.5194/acp-14-1663-2014

Townsend-Small, A., Tyler, S. C., Pataki, D. E., Xu, X., & Christensen, L. E. (2012). Isotopic measurements of atmospheric methane in Los Angeles, California, USA: Influence of "fugitive" fossil fuel emissions. *Journal of Geophysical Research*, *117*, D07308. https://doi.org/10.1029/2011JD016826

Turnbull, J. C., Karion, A., Fischer, M. L., Faloona, I., Guilderson, T., Lehman, S. J., et al. (2011). Assessment of fossil fuel carbon dioxide and other anthropogenic trace gas emissions from airborne measurements over Sacramento, California in spring 2009. *Atmospheric Chemistry and Physics*, *11*(2), 705–721. https://doi.org/10.5194/acp-11-705-2011

Ussiri, D. A. N., Lal, R., & Jarecki, M. K. (2009). Nitrous oxide and methane emissions from long-term tillage under a continuous corn cropping system in Ohio. *Soil and Tillage Research*, *104*(2), 247–255. https://doi.org/10.1016/j.still.2009.03.001

Vardag, S. N., Gerbig, C., Janssens-Maenhout, G., & Levin, I. (2015). Estimation of continuous anthropogenic CO_2: Model-based evaluation of CO_2, CO, $\delta^{13}C(CO_2)$ and $\Delta^{14}C(CO_2)$ tracer methods. *Atmospheric Chemistry and Physics*, *15*(22), 12705–12729. https://doi.org/10.5194/acp-15-12705-2015

Verhulst, K. R., Karion, A., Kim, J., Salameh, P. K., Keeling, R. F., Newman, S., et al. (2017). Carbon dioxide and methane measurements from the Los Angeles Megacity Carbon Project—Part 1: Calibration, urban enhancements, and uncertainty estimates. *Atmospheric Chemistry and Physics*, *17*(13), 8313–8341. https://doi.org/10.5194/acp-17-8313-2017

Wang, D., Chen, Z., & Xu, S. (2009). Methane emission from Yangtze estuarine wetland China. *Journal of Geophysical Research*, *114*, D08113. https://doi.org/10.1029/2008JG000857

Wang, J., Pan, X., Liu, Y., Zhang, X., & Xiong, Z. (2012). Effects of biochar amendment in two soils on greenhouse gas emissions and crop production. *Plant and Soil*, *360*(1–2), 287–298. https://doi.org/10.1007/s11104-012-1250-3

Wang, R., Tao, S., Ciais, P., Shen, H. Z., Huang, Y., Chen, H., et al. (2013). High-resolution mapping of combustion processes and implications for CO_2 emissions. *Atmospheric Chemistry and Physics*, *13*(10), 5189–5203. https://doi.org/10.5194/acp-13-5189-2013

Wang, Y., Munger, J. W., Xu, S., McElroy, M. B., Hao, J., Nielsen, C. P., & Ma, H. (2010). CO_2 and its correlation with CO at a rural site near Beijing: Implications for combustion efficiency in China. *Atmospheric Chemistry and Physics*, *10*(18), 8881–8897. https://doi.org/10.5194/acp-10-8881-2010

Wolf (2011). *China and India, 2025: A comparative assessmen*, (Vol. 7).

Wong, K. W., Fu, D., Pongetti, T. J., Newman, S., Kort, E. A., Duren, R., et al. (2015). Mapping CH_4: CO_2 ratios in Los Angeles with CLARS-FTS from Mount Wilson California. *Atmospheric Chemistry and Physics*, *15*(1), 241–252. https://doi.org/10.5194/acp-15-241-2015

Wu, K., Lauvaux, T., Davis, K. J., Deng, A., Lopez Coto, I., Gurney, K. R., & Patarasuk, R. (2018). Joint inverse estimation of fossil fuel and biogenic CO2 fluxes in an urban environment: An observing system simulation experiment to assess the impact of multiple uncertainties. *Elementa Science of the Anthropocene*, *6*(1). https://doi.org/10.1525/elementa.138

Wunch, D., Toon, G. C., Hedelius, J. K., Vizenor, N., Roehl, C. M., Saad, K. M., et al. (2016). Quantifying the loss of processed natural gas within California's South Coast Air Basin using long-term measurements of ethane and methane. *Atmospheric Chemistry and Physics*, *16*(22), 14091–14105. https://doi.org/10.5194/acp-16-14091-2016

Xiao, Y., Jacob, D. J., Wang, J. S., Logan, J. A., Palmer, P. I., Suntharalingam, P., et al. (2004). Constraints on Asian and European sources of methane from CH_4-C_2H_6-CO correlations in Asian outflow. *Journal of Geophysical Research*, *109*, D15S16. https://doi.org/10.1029/2003JD004475

Xu, J., Lee, X., Xiao, W., Cao, C., Liu, S., Wen, X., et al. (2017). Interpreting the $^{13}C/^{12}C$ ratio of carbon dioxide in an urban airshed in the Yangtze River Delta China. *Atmospheric Chemistry and Physics*, *17*(5), 3385–3399. https://doi.org/10.5194/acp-17-3385-2017

Yan, X., Akiyama, H., Yagi, K., & Akimoto, H. (2009). Global estimations of the inventory and mitigation potential of methane emissions from rice cultivation conducted using the 2006 Intergovernmental Panel on Climate Change guidelines. *Global Biogeochemical Cycles*, *23*, GB2002. https://doi.org/10.1029/2008GB003299

Yan, X., Cai, Z., Ohara, T., & Akimoto, H. (2003). Methane emission from rice fields in mainland China: Amount and seasonal and spatial distribution. *Journal of Geophysical Research*, *108*(D16), 4505. https://doi.org/10.1029/2002JD003182

Zhang, B., & Chen, G. Q. (2010). Methane emissions by Chinese economy: Inventory and embodiment analysis. *Energy Policy*, *38*(8), 4304–4316. https://doi.org/10.1016/j.enpol.2010.03.059

Zhang, G., Yu, H., Fan, X., Yang, Y., Ma, J., & Xu, H. (2016). Drainage and tillage practices in the winter fallow season mitigate CH_4 and N_2O emissions from a double-rice field in China. *Atmospheric Chemistry and Physics*, *16*(18), 11853–11866. https://doi.org/10.5194/acp-16-11853-2016

Zhang, W., Zhang, Q., Huang, Y., Li, T. T., Bian, J. Y., & Han, P. F. (2014). Uncertainties in estimating regional methane emissions from rice paddies due to data scarcity in the modeling approach. *Geoscientific Model Development*, *7*(3), 1211–1224. https://doi.org/10.5194/gmd-7-1211-2014

Zhao, L., Lee, X., & Liu, S. (2013). Correcting surface solar radiation of two data assimilation systems against FLUXNET observations in North America. *Journal of Geophysical Research: Atmospheres*, *118*, 9552–9564. https://doi.org/10.1002/jgrd.50697

Zhu, T., Bian, W., Zhang, S., Di, P., & Nie, B. (2017). An improved approach to estimate methane emissions from coal mining in China. *Environmental Science & Technology*, *51*(21), 12072–12080. https://doi.org/10.1021/acs.est.7b01857